Photoemission electron microscopy of localized surface plasmons in silver nanostructures

Experiments and simulations

Robin Svärd

LUND
UNIVERSITY

A thesis presented for the degree of
Master of Science in Physics
Project duration: 13 months

Supervisor: Prof. Anders Mikkelsen
Co-supervisors: Erik Mårsell, M.Sc.
Arthur Losquin, Ph.D.

Division of Synchrotron Radiation Research
Department of Physics
Sweden
May 2015

Abbreviations

UHV	Ultra–high vacuum
PEEM	Photoemission electron microscope
FDTD	Finite–difference time–domain
LSP	Localized surface plasmon
PE	Photoemission
MPPE	Multi–photon photoemission
LSPR	Localized surface plasmon resonance
DFT	Discrete Fourier Transform
PML	Perfectly matched layer
IS	Integral sample stage
MCP	Micro–channel plate
CCD	Charge–coupled device
IR	Infrared
d-scan	Dispersion scan
FoV	Field–of–view
ITO	Indium tin oxide
SEM	Scanning electron microscope

Acknowledgments

I want to thank my supervisor, professor Anders Mikkelsen, for once upon a time igniting my interest in solid state physics that came to lead me down my current path. I also want to thank my two co-supervisors, Erik Mårsell and Arthur Losquin, for making this diploma work possible and guiding me throughout the entire project.

Due to being involved in such a cross–disciplinary field of study, I got the opportunity to work with many different people. For that I am very grateful, and would like to thank the attosecond group over at Atomic physics who endlessly kept the laser happy during the experiments. Anne L'Huillier, Miguel Miranda, Chen Guo, Anne Harth and Elenora Lorek, thank you, and I am sure you will get the XUV setup running eventually!

I also want to thank all the remaining colleagues at the division of Synchrotron Radiation Research, for all the scientific and "högt i tak" discussions that tend to come with the lunch breaks.

Last but not least, I would like to thank my friends, family and co–workers outside of Fysicum for bearing with my ever–failing attempts of explaining what I am actually working with.

Photoemission electron microscopy of localized surface plasmons in silver nanostructures

Experiments and simulations

Robin Svärd

Abstract

In this work, spatially resolved localized surface plasmons (LSPs) in individual silver nanocubes and nanoellipsoids are imaged with a photoemission electron microscope (PEEM). Using broadband laser pulses with photon energies below the work function threshold of the material, multiphoton photoemission (MPPE) processes coupled to the LSPs governs the strong enhancement of the plasmonic near-field detected in the PEEM.

For the nanocubes, the dependence of photoemission (PE) yield on laser polarization is investigated, and it is found that the local enhancement of the plasmonic near–field strongly depends on a superposition of localized plasmon modes excited in the nanocube. For the nanoellipsoids, the near–field dynamics are investigated using few–cycle laser pulses in an interferometric pump–probe setup, and it is found that the near–fields at the two ends of a particle dephase on a sub–3 fs timescale due to plasmon retardation across the particle. For both types of nanostructures, the results are supported by finite–difference time–domain electrodynamics simulations.

The outcome of the work presented in this report, for both the nanocubes and nanoellipsoids, will be the source of future publication(s).

Robin Svärd

Ytplasmoner — Små, snabba och otroligt användbara

Människan har länge förundrats över de vackra färgerna som klär glasrutorna i många medeltida katedraler, men det var dock inte förrän år 1957 då en forskare vid namn Rufus Richie först föreslog vad som gav upphov till detta fenomen. Det visade sig vara en egenskap hos *ytplasmoner*, som bl.a. har en kraftig förmåga att absorbera eller reflektera infallande ljus.

Deras speciella egenskaper gör ytplasmoner väldigt intressanta för forskning, och potentiella användningsområden finns inom både fysik, kemi, biologi och elektronik. Som namnet antyder uppkommer ytplasmoner precis på ytan mellan en metall och ett isolerande material. En väldigt viktig egenskap hos ytplasmoner är att de kan koncentreras ner till mycket små områden, ungefär i storleksordningen ett par hundra nanometer (en nanometer är en miljarddels meter). Ett hinder med ytplasmoner är dock att de är otroligt kortlivade, ofta bara ett fåtal femtosekunder (en femtosekund är en miljondels miljarddels sekund). För att vi över huvud taget ska kunna studera dessa processer krävs därför instrument med väldigt hög upplösning både i tid och rum.

I det här arbetet har vi undersökt ytplasmoner på nanostrukturer av silver med hjälp av ett *fotoemissionselektronmikroskop*. När en yta träffas av ljus kan den släppa loss elektroner, och dessa elektroner samlas sedan in av mikroskopet för att skapa en kraftigt förstorad bild av ytan. Ljuset som träffar ytan produceras i ultrakorta laserpulser vars egenskaper vi dessutom kan variera efter behov för att studera olika typer av växelverkan med ytan. Kombinationen av elektronernas förmåga att avbilda korta längdskalor och laserpulsernas förmåga att följa processer på otroligt korta tidsskalor gör det därför möjligt att ta bilder på själva ytplasmonerna.

Det främsta sättet att kontrollera ytplasmoner är genom att variera nanostrukturens storlek och form. Detta arbete har därför fokuserat på två olika typer av silverstrukturer — kuber och ellipsoider.

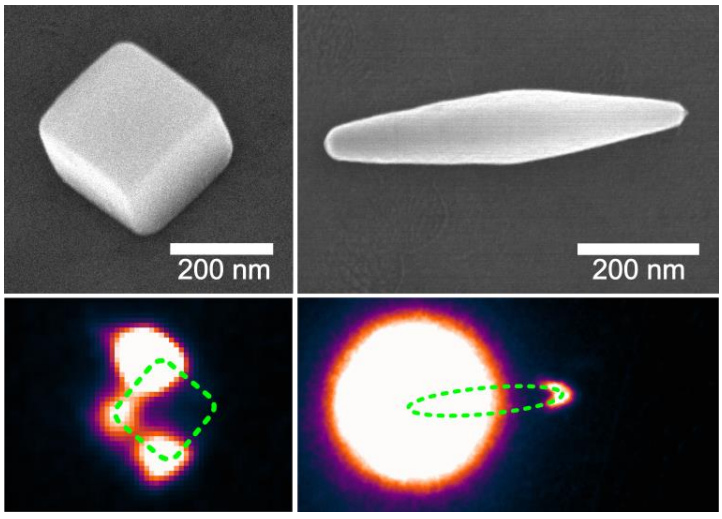

Handledare: Prof. Anders Mikkelsen
Biträdande handledare: Erik Mårsell och Arthur Losquin
Examensarbete 60 hp i Fysik 2015
Avdelningen för Synkrotronljusfysik,
Fysiska instutitionen, Lunds Universitet

Contents

Chapter 1

Introduction

Mankind has been fascinated by plasmons for hundreds of years without actually knowing what they are. One of the most reheated examples is the historic stained glass found in many medieval cathedrals, whose vivid colors originate from light interacting with metal nanoparticles. However, it was not until 1957 that Rufus Ritchie first suggested the existence of the phenomena [1]. With pioneers such as Andreas Otto [2] and Erich Kretschmann [3], it would then only take a few years before the first plasmon–based applications began to arise.

During the same time, in 1959, renowned physicist Richard Feynman discussed in his talk *There's plenty of room at the bottom* [4] the concept of artificially tailoring materials via direct manipulation of their constituents, namely the atoms. It is arguably this discussion that acted as the catalyst which sparked the widespread interest in nanotechnology. Since then, it did not take long until various techniques that allowed for the fabrication of nanostructures to emerge, especially in the semiconductor industry.

Much of the strong interest in nanotechnology originates from the fact that many materials drastically change their properties at a small enough scale. One such phenomenon is related to the optical properties of nanostructures, where the interactions of photons and the metallic surface can give rise to so–called surface plasmons. Surface plasmons are essentially coherent electron oscillations which emerge at the interface between a metal and a dielectric when subject to radiation. In many cases, this results in a greatly enhanced electromagnetic field close to the surface of the structure.

Being a field often said to bridge optics and electronics, plasmonics have attracted much attention in recent years due to their many potential applications and can be found

in research areas such as second harmonic generation [5], chemical or biological sensing [6] and surface–enhanced Raman spectroscopy [7]. In order for plasmons to be excited, the material needs to have free electrons. Noble metals, such as silver, with a high electron density are particularly suitable. Additionally, silver can be tailored into a myriad of different nanostructures. With the most powerful way to tune the excitation of plasmons being through control of shape and size of the nanoparticle [8], this makes silver even more favored.

In 1960, the invention of the laser [9] came to revolutionize both the physics community and everyday life. As a result of the coherent nature of laser radiation, its light can be emitted in very short bursts. With the typical lifetime of surface plasmons being just a few femtoseconds, very short light pulses are thus required for certain types of plasmonic studies. Recently, the emergence of ultrafast lasers has allowed for real–time studies of processes with extreme temporal resolution through so–called pump–probe experiments [10]. The method relies on exciting the material with an initial light pulse and subsequently probing the state of the system with a second light pulse. This process will take a snapshot of the system at a given time, and in varying the delay between the two pulses, a temporal recording of its evolution can be mapped out.

1.1 Overcoming the Abbe diffraction limit

All different types of imaging instruments, from telescopes to microscopes, are fundamentally limited by diffraction. This was realized in 1873 by Ernst Abbe, who came to formulate the relation

$$d = \frac{\lambda}{2NA} \tag{1.1}$$

where d is the minimum distance between two observed objects for them to be resolved separately, λ is the wavelength of the input signal and NA is called the numerical aperture related to the optics of the instrument ($0 < NA < 1$). Essentially, this means that the input signal must have a wavelength that is at least smaller than twice the structure it is meant to probe. Conventional optical microscopes which operates using visible light (400 to 700 nm) will thus be unable to resolve features separated by less than a few hundred nanometers. This fact immediately poses a problem when it comes to imaging nanostructures. In order to circumvent the diffraction limit, one would either have to

resort to using light of a much shorter wavelength or simply use some other kind of input signal, such as electrons.

There are different ways to probe the surface of materials, one of them being based on the effect of light–matter interaction first presented by Heinrich Hertz in 1887 [11], which later led Albert Einstein in 1905 to formulate his explanation of why only photons of a certain energy were capable of knocking electrons out of matter. This phenomenon, now generally known as the photoelectric effect, resulted in Einstein being awarded with the Nobel prize in physics in 1921 [12].

Utilizing this phenomenon, the first ultrahigh–vacuum photoemission electron microscope (UHV PEEM) was designed in 1963 by G. F. Rempfer. A PEEM is capable of generating images by capturing the emitted photoelectrons, creating a greatly magnified image of the surface of the sample. Additionally, these images will also reveal contrast differences depending on local variations in the electron emission of the sample. Contrast differences might originate from different causes, such as crystal structure variations or enhanced fields close to the surface. Experiments can be carried out using a number of different excitation sources, from laser light to synchrotron radiation, making the PEEM a very versatile instrument. Additionally, the detected photoelectron signal can be very high which allows for short image acquisition times and, in some cases, even video rate imaging.

1.2 Motivation

Understanding the interactions between light and metal nanoparticles giving rise to surface plasmons is not an easy task, especially if the ulterior goal is complete control over the response. However, amongst the many things that can be imaged in a PEEM, plasmons happens to be one of them.

A primary purpose of this diploma work is to investigate the enhanced near–fields in silver nanostructures in the time–domain. By combining ultrafast lasers for temporal resolution with the detection of electrons for spatial resolution, a characterization of the near-fields and how they can be controlled will be carried out. Additionally, parallel to the experiments, finite–difference time–domain (FDTD) electrodynamics simulations will be utilized to later compare with the experimental data.

The long–term goals for this research are diverse, such as replacing electrons as information carriers with surface plasmons or use the light–matter interactions as logic gates in devices. What they all have in common, however, is a dependency of an imaging technique capable of recording processes with an extreme spatiotemporal resolution.

Chapter 2

Theory and techniques

In this chapter, the most important concepts to which all experimental results are connected will be presented. First, a short introduction to photoemission electron microscopy will be discussed. This is followed by a mathematical and conceptual view of plasmons at solid surfaces, including the localized surface plasmon (LSP), which is the primary phenomenon of our observations. Finally, the numerical simulation method known as finite–difference time–domain (FDTD) will be introduced.

2.1 Photoemission electron microscopy

In photoemission electron microscopy, electrons emitted from a sample through photo–ionization are used to create an image. Using a high voltage, the emitted photoelectrons are accelerated and guided through electrostatic lenses in order to form a greatly magnified image of the surface of the sample. With the photon in–electron out approach, it is possible to circumvent the diffraction limit of light. Allowing illumination of the entire field–of–view, this imaging technique provides full–field microscopy images with real–time acquisition. Depending on how the incident light interacts with the sample, local variations in electron emission generates contrast in the image.

Once the instrument is properly aligned and most resolution limiting aberrations are accounted for, it is important to note that the measured photoemission (PE) yield in a PEEM will be highly directional. The yield will almost exclusively be composed of photoelectrons emitted normal to the sample plane, and if a structure does not emit any electrons whatsoever, it is essentially invisible. For more information and specifications related to the instrument used during the experiments, see section 3.1.

2.1.1 Light–matter interaction: the photoelectric effect

Should a photon interact with an atom, there is a certain probability that the photon is completely absorbed, transferring all of its energy to the atomic system. This interaction can cause the matter to be excited, leaving an electron in a higher energy empty state, or, should the absorbed energy be high enough, cause the electron to completely leave the system instead. The first person to understand and explain this phenomenon was Albert Einstein, who came to realize that the energy of photons is quantized. The photoelectric effect is usually described by

$$E_{kin} = \hbar\omega - E_B - \phi \tag{2.1}$$

where E_{kin} is the kinetic energy of the emitted photoelectron, $\hbar$ is the Dirac constant, ω is the radiation frequency of the incident photon, E_B is the binding energy of the electron relative to the Fermi level, and ϕ is the work function relating the vacuum level to the Fermi level of the solid. In order for the photoelectric effect to occur, the incident photon must have an energy $\hbar\omega$ that is greater than the work function threshold of the material, with the excess photon energy being transferred to the electron as E_{kin}. An electron emitted due to absorption of a photon is referred to as a photoelectron and for a metal, the work function is typically in the order of 3–6 eV.

2.1.2 Multi–photon photoemission

So far, photoemission has only been considered for the linear regime. With a sufficiently strong electromagnetic field, non–linear processes may instead become dominant. In the non–linear regime, additional terms will emerge that correspond to multiple photons interacting with the system. As a consequence, there are exceptions to the rule that the energy of the incident photon must be greater than the work function threshold for photoemission to occur. In order to conceptually explain this process, the idea of virtual states is introduced. Should the photon energy be lower than the work function of the material, there is still a probability, albeit a very small one, that the photon will be absorbed and an electron can momentarily be promoted to an intermediate virtual state somewhere in between two bound states. Once in an excited virtual state, the electron can absorb yet another photon resulting in even further excitation. This process could in theory carry on indefinitely, until the electron completely decouples from the system through ionization.

This is referred to as multi–photon photoemission (MPPE), and a simplified schematic of the process is shown in fig 2.1.

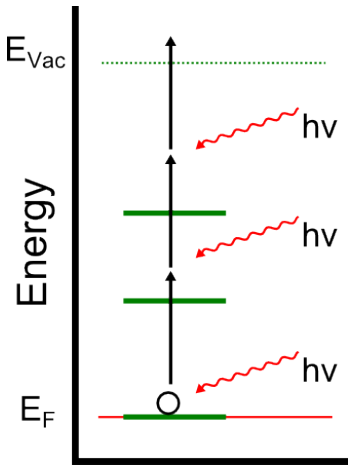

Figure 2.1: Illustration of a 3–photon photoemission process. E_{F} denotes the Fermi level of the atom and E_{Vac} the vacuum level.

Further, the life–time τ of a virtual state is short enough not to violate the time–energy uncertainty relation [13]

$$\tau \Delta E \geq \frac{\hbar}{2} \tag{2.2}$$

where ΔE is the energy difference to the nearest bound state. Thus, in order for a second or third photon to be absorbed before the virtual state decay, a high enough photon flux is an absolute necessity. This is usually achieved using pulsed lasers as the excitation source due to their potentially high intensity. Nonetheless, it is important to remember that MPPE is a non–linear process. As such, the photoemission yield is not necessarily doubled if the intensity of the light is. However, since MPPE is heavily influenced by the electric field strengths involved, it makes it particularly useful for studies of surface near–fields, which can be significantly enhanced by plasmons.

2.2 Plasmonics

When an incident photon interacts with a conducting material, photoemission is not the only phenomenon that can occur. In the field of plasmonics, the conduction electrons of a material are studied as they are collectively influenced by electromagnetic radiation. An excited cloud of free electrons is often considered a plasma. When the electrons in a material are displaced, they are immediately subjected to an attractive force trying to pull them back to their initial positions due to the positive charge left behind (the nucleus).

This results in a collective oscillation of the electron gas at a specific frequency that is driven by the excitation.

As mentioned earlier, plasmonics lies on the border between optics and electronics. The interaction between a metal and light can give rise to a certain type of plasmon, more specifically called a surface plasmon. Before going into detail of what a surface plasmon is, some general background to the optical properties of metals will be discussed.

2.2.1 Optical properties of metallic structures

Since plasmons are described as the oscillation of a classical electron gas, most of their properties can be derived directly from the macroscopic set of Maxwell's equations. Named after James Clerk Maxwell, who summarized a set of partial differential equations that describe the interactions between electric and magnetic fields, the equations are often portrayed as

$$\begin{aligned} \nabla \cdot \vec{D} &= \rho \\ \nabla \cdot \vec{B} &= 0 \\ \nabla \times \vec{E} &= -\frac{\partial \vec{B}}{\partial t} \qquad (2.3) \\ \nabla \times \vec{H} &= \vec{J} + \frac{\partial \vec{D}}{\partial t} \qquad (2.4) \end{aligned}$$

where ρ and $\vec{J}$ are the electric charge and current density, respectively, $\vec{B}$ is the magnetic flux density, and $\vec{E}$ and $\vec{H}$ are the electric and magnetic fields. $\vec{D}$, here described as the dielectric displacement field, can also be expressed as $\vec{D} = \varepsilon_0 \varepsilon \vec{E}$, where ε_0 is the permittivity of vacuum and $\varepsilon(\omega)$ is the dielectric function of a material.

As materials are subject to electromagnetic radiation, the dielectric function of the material dictates how it will react. While the dielectric function can depend on variables such as polarization of the light, it has an exceptional frequency dependency which, for simplicity, will be the only parameter considered henceforth. The dielectric function is composed of two quantities, one real (ε_1) and one imaginary (ε_2), as

$$\varepsilon(\omega) = \varepsilon_1(\omega) + i\varepsilon_2(\omega). \qquad (2.5)$$

ε_1 describes how electrically polarized the material becomes due to the applied oscillating field, while ε_2 describes how well the material absorbs certain frequencies of the incident

radiation. For plasmons, the ways that a material can be electrically polarized is exceptionally important, as the polarization provides the main restoring force for the electron oscillations [14]. Considering the conduction electrons of a metal as a free electron gas, then the dielectric function can be expressed as

$$\varepsilon(\omega) = 1 - \frac{\omega_p^2}{\omega^2} \tag{2.6}$$

where ω_p is called the plasma frequency of the material. Each material has a characteristic plasma frequency, corresponding to how strong the restoring force is if the electrons in the gas are displaced. As will be discussed, the plasma frequency plays an important role for the excitation of plasmons.

2.2.2 Localized surface plasmons

At the interface between materials with positive and negative real parts of the dielectric function, there exist solutions to Maxwell's equations. More specifically, these solutions are confined only to the surface of the material. As can be seen from equation 2.6, the real part of the dielectric function for metals will take on negative values for frequencies below the plasma frequency. At the interface between a conductor and a dielectric, this will show up as surface–confined modes, typically referred to as the before–mentioned surface plasmon. After excitation, the surface plasmons propagate along the interface between the conductor and the dielectric and are evanescently confined perpendicular to their direction of propagation, much like ripples in a pond of water. Thus, a surface plasmon can be described as the collective oscillation of a free electron gas density at a metallic interface and is often described as surface waves as shown in fig. 2.2.

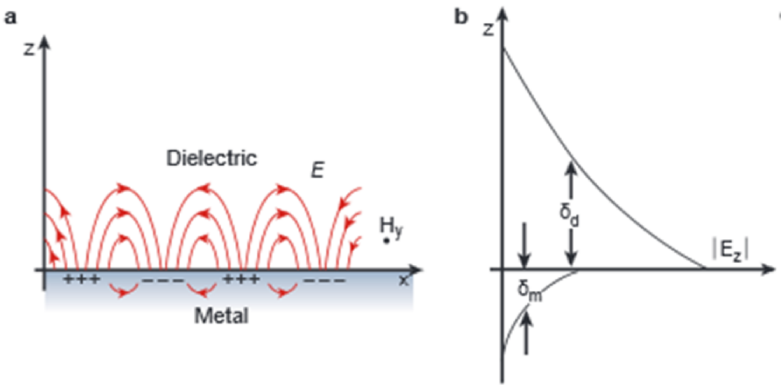

Figure 2.2: a) Surface plasmon propagating along the interface of a metal and a dielectric. b) The field in the perpendicular direction decay evanescently. Retrieved from ref. [15].

However, for nanoparticles with distinct boundaries, localized surface plasmons (LSP) confined within the structure may be excited instead. Due to the confinement, should the frequency of the collective oscillation match that of the driving field, a resonance will emerge. These resonances are called localized surface plasmon resonances (LSPR) and exists within the visible region of the electromagnetic spectrum for *e.g.* gold and silver nanoparticles. A feature of the localized surface plasmons is that they can be focused down to very small regions, and at the resonances, couple strongly to external electromagnetic fields. How the LSPs are related to the absorption and scattering of light dictates the optical properties of the nanoparticle and there are generally two regions where surface plasmons can be studied, either in the near–field or in the far–field. In analogy to the electromagnetic fields around a transmitting antenna, the near–field is defined as the region close to the surface where the fields are evanescent, while the far–field is defined as the light scattered off the particle which behaves as plane waves.

In the far–field, the LSPs show up as enhanced absorption or scattering of light and can visibly be observed as bright colors exhibited by the particles. In the near–field, however, the LSP electromagnetic fields decrease with the cube of the distance, which thus can give rise to greatly enhanced fields very close to the surface once excited. For individual particles, the near–field enhancement has been reported to be as large as two orders of magnitude relative to the amplitude of the incident radiation [16]. Since the presence of LSPs will greatly enhance the electric fields at certain areas of the surface depending on the resonance, MPPE will be strongly favored in localized parts of the nanostructure.

Additionally, the restoring Coulomb interactions force the LSPs to obey certain conditions based on the geometry of the nanostructures. As a result, only discrete modes are allowed to be excited, much like standing waves. For nanostructures approaching the electrostatic limit ($d \ll \lambda$), only the lowest possible order resonance can be excited, namely the dipolar mode. The number of possible resonances then increases as the number of ways that the particle can be polarized increases. By changing the size of the nanoparticle, studies have shown that a LSPR can be tuned across a wide spectroscopic range [17].

Since many experimentally realizable nanostructures are larger than their electrostatic limit (when using visible light as the excitation source), different modes can be excited in the structures. This introduces another topic, which is important to consider when studying LSPs. Modes excited in a nanostructure can be classified as either 'bright' or

'dark'. For bright modes, the overall charge distribution result in a finite dipole moment, *e.g.* the dipolar mode. Because of this, they can couple strongly to light and decay into the far–field in the normal direction, making them ideal for light scattering studies. Dark modes, on the other hand, possess zero dipole moment, and do not radiate into the far–field in the normal direction, *e.g.* the quadrupolar mode. However, using a photon in–electron out approach, such as the PEEM, even the dark modes can be investigated due to the technique only being sensitive to the near–field. Further, under normal incidence, the optical excitation of dark LSPs is also forbidden due to symmetry, although they can still be excited using oblique incidence [18]. Bright and dark longitudinal modes are most easily demonstrated for quasi–one dimensional structures, such as those shown in fig. 2.3.

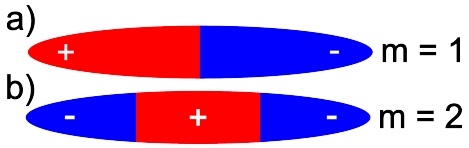

Figure 2.3: Sketches of the instantaneous charge distributions for a) the bright dipolar ($m = 1$) mode with a net dipole moment and b) the dark quadrupolar ($m = 2$) mode with zero dipole moment.

2.3 Finite–Difference Time–Domain

The first person to rigorously study the scattering of light by metal nanoparticles was Gustav Mie, who in 1908 came to formulate Mie theory which described the LSP modes for metal colloids [19]. However, LSPs can be solved analytically only for very simple shapes, such as spheres or ellipsoids. Even then, Gustav Mie's paper contained no less than 102 sets of equations to completely explain the scattering properties of spheres. In order to obtain accurate optical properties for metal nanoparticles of arbitrary geometries, full electromagnetic solvers are required. These numerical techniques are all based on solving the Maxwell equations, and one of them is called finite–difference time–domain (FDTD). A more elaborate explanation of how the FDTD method updates the electromagnetic fields in a simulation volume is described in detail elsewhere [20, 21], however, the key features will be summarized in the following sections.

2.3.1 General concepts

The FDTD method deals directly with the two curl equations of the Maxwell equations, or more specifically, Faraday's (eq. 2.3) and Ampere's laws (eq. 2.4). In order to evaluate the spatial and temporal derivatives, it employs finite differences as approximation. This is achieved by a discretization of both time and space. For simplicity, all fields are set to zero at time zero. This way, it is possible to completely neglect the two divergence equations as they are contained within the curl equations due to the initial boundary conditions [20].

Space is discretized into a grid composed of rectangular unit cells based on a formulation first presented by Kane Yee in 1966 [22]. In 3D, the boundaries of these so–called Yee cells are where the electromagnetic fields are calculated and are shown schematically in fig. 2.4. More specifically, the electric field components form the edges of the cube while the magnetic field components form the faces of the cube. Each cube is also assigned a permittivity and a permeability based on what type of material it is supposed to model. Specifically due to the discretization of space, the FDTD method allows for full electrodynamic studies of arbitrary geometries.

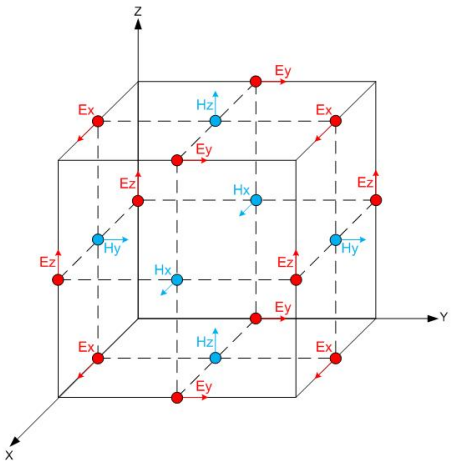

Figure 2.4: The Yee cell formulation, showing where the electric and magnetic fields are evaluated. Retrieved from ref. [23].

In short, after discretizing time and space, the two curl equations giving the unknown future fields can be expressed solely in terms of known past fields. Due to the initial boundary conditions, there exist solutions to the equations. In fact, for each time step, the algorithm uses one type of field to advance the other [21]. This process is then repeated until a desired duration has elapsed or all the fields either dissipates or reach a steady–

state. Additionally, since FDTD is a time–domain method, a broadband excitation can be injected, resulting in the response over a wide range of frequencies from a single simulation. During the course of a simulation, the electromagnetic fields can be sampled and recorded from specific Yee cells corresponding to the areas of interest.

For the current work, due to only being concerned with the near–field response of the nanostructures when imaging in a PEEM, it is arguably only the absorption of light that is of interest. Since the net power flowing into a box enclosing a modeled structure is known from the injected excitation source, anything that leaves the volume will thus be a measure of the absorbed frequencies. Thus, the absorption cross–section as a function of frequency of a structure is obtained by running a Fourier transform of the net power flowing out of the volume, and can be used as a means to locate resonances in the structure. A resonance will show up as greatly enhanced absorption, and the number of resonances supported in a structure depends on its geometry. Once a resonance has been located, a Discrete Fourier Transform (DFT) of the electric fields can be calculated at the specific frequency, resulting in a steady–state field distribution for that resonance.

It is also possible to estimate the PE yield for an actual PEEM image based on the electromagnetic response from a simulated structure. If one assumes nth order MPPE processes, then the measured intensity would be proportional to the electric field raised to the power of $2n$ ($I \propto E^{2n}$) [24]. Recalling that the photoemission (PE) yield $Y(\vec{r})$ measured in the PEEM is almost exclusively originating from electrons being emitted normal to the sample plane, it is enough to consider only the z–component of the simulated electric fields. Hence, by evaluating each point in space as

$$Y_z(\vec{r}) \propto \int_{-\infty}^{\infty} |\vec{E}_z(\vec{r}, t)|^{2n} \mathrm{d}t \tag{2.7}$$

where $\vec{E}_z(\vec{r}, t)$ is the near–field response induced by the excitation source, the resulting image should correspond to what an actual PEEM image could look like.

2.3.2 Simulation limitations

Being a completely numerical method, FDTD simulations have certain limitations and artifacts. It is important to remember that while versatile, the algorithms that FDTD utilizes are inherently approximate. The accuracy of a simulation is directly related to the

size of the Yell grid cells since they must be fine enough to resolve the smallest geometrical features. As a consequence, high accuracy often leads to long simulation times and a lot of required computational memory.

Due to computational memory constraints, the simulation volume itself also has to be limited. In order to simulate how the fields dissipate into infinity, the outer boundaries are often closed with so–called Perfectly Matched Layers (PML). A PML simply acts as a very lossy material, effectively absorbing the fields as they leave the simulation volume. It is important to actively minimize fields being reflected back into the simulation volume from the outer boundaries, as they would otherwise induce non–physical fluctuations in the electromagnetic fields. This is best accounted for by increasing the number of PMLs.

Modeling the dielectric function of a material over a wide range of frequencies is a further restraint. For many metals in the visible part of the electromagnetic spectrum, rapid fluctuations exist which makes them hard to properly represent in a model. Nonetheless, despite these limitations, the FDTD model has proven to be particularly useful for a wide range of purposes, including the simulation of plasmons [25].

Chapter 3

Experimental setup and simulation methods

In this chapter, the experimental setup used during this project including a more in–depth description of the PEEM and the different types of light sources will be presented. Additionally, some information regarding how the FDTD simulation software was implemented will be discussed, as well as how the measured data were post–processed and subsequently analyzed.

3.1 Focus IS-PEEM

The Focus IS–PEEM used throughout this project belongs to a family of cathode lens microscopy instruments, manufactured by Focus GmbH and is capable of providing a best–case lateral resolution of 20 nm. The sample stage of the PEEM is an integral, piezoelectrically driven stage (IS), and the samples themselves act as the cathode and are thus considered as being part of the objective lens. While these types of sample stages greatly increase the overall stability by negating any relative motion between the sample and the rest of the objective lens, they also limit the sample to only be moved in the sample plane itself.

Due to the mean–free path of emitted photoelectrons being extremely short, in the range of just a few Å in air, ultra–high vacuum (UHV) has to be maintained at all times during PEEM imaging. This is achieved through a combination of a turbo pump and an ion pump. The main chamber, operating at a base pressure of 10^{-9} mbar, is separated

from the transfer chamber, allowing an exchange of samples without having to vent the entire system. It is also covered in a μ–metal shielding which prevents external magnetic fields from interfering with the imaging. The shielding has a number of holes through which the sample can be seen and/or illuminated, however, these are positioned at a 25° angle with respect to the sample plane, resulting in any incident light hitting the sample at a grazing angle. Fig. 3.1 shows a simplified schematic of the PEEM.

After illuminating the sample, which is kept at ground potential, emitted photoelectrons are accelerated by an applied large positive bias to an extractor positioned roughly 1.8 mm in front of the sample. Following the extractor, a focal and column electrode together make up an electrostatic tetrode objective lens, whose focal length is primarily determined by the voltage applied to the focal electrode and whose magnification is determined by the voltage ratio between the extractor and column electrode [26].

In the back–focal plane of the objective lens, a piezoelectrically driven mount with five different contrast apertures of diameters ranging from 30 μm to 1.5 mm can be used to physically block some of the emitted photoelectrons. A smaller aperture allows for higher resolution at the cost of intensity as the number of divergent electrons are minimized. Behind the contrast apertures, an octupole stigmator and deflector allows for manual minimization of astigmatism and centering of the photoelectrons on the optical axis. This is followed by an iris which was never changed during the present work.

Further into the microscope column, two einzel lenses allow for different modes of operation. An einzel lens consists of three cylindrical tubes, where the potential of the middle tube differs from the two outer tubes, which in turn results in an electrostatic saddle point that focuses the electrons towards the optical axis. Hence, the more lenses that are active, the greater the maximum possible magnification of the image. Depending on how many lenses that are currently active, the microscope operates in one–, two– (fig. 3.1a) or three–lens mode (fig. 3.1b), respectively. Additionally, the PEEM is equipped with an energy filter for spectromicroscopy purposes, although it was not used in the present work. The PEEM is controlled via a handheld control unit supplied by the manufacturer in conjunction with a software.

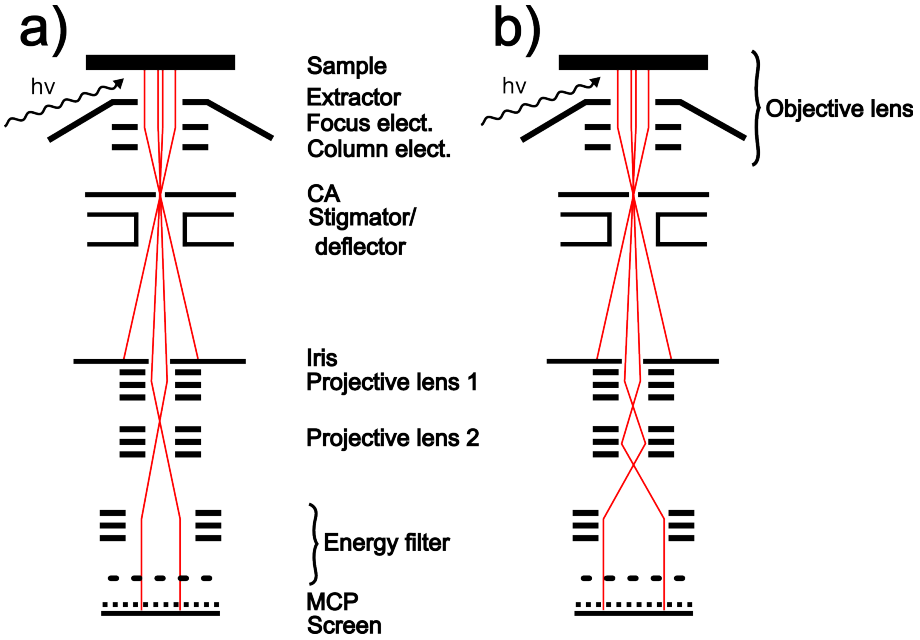

Figure 3.1: Schematic overview of the PEEM, where the most crucial parts have been pointed out. a) The PEEM operating in two–lens mode. b) The PEEM operating in three–lens mode.

3.1.1 Imaging assembly

The first part of the imaging assembly of the PEEM is a micro–channel plate (MCP) detector, capable of amplifying an electron signal several orders of magnitude. While it behaves similarly to an electron multiplier in the sense that it amplifies an electron signal, the main difference is that an MCP simultaneously provides spatial resolution due to it containing many separate channels. However, the MCP is a very delicate piece of equipment, and utmost precautions must be taken when changing PEEM imaging settings to avoid damaging it. The multiplied electrons are then accelerated onto a YAG single crystal, whereupon the emitted light can be detected by a charge–coupled device (CCD) camera positioned behind the screen.

Two different CCD cameras were used throughout this project depending on what types of measurements were carried out. The first is a commercially available PCO Pixelfly PF–M–QW[1], most suitable for bright light conditions such as when illuminating with a Hg lamp which is described in section 3.1.3. Its low exposure times allowed video–rate imaging of the sample, however, lacking active cooling, thermal noise would cause any longer exposures of small field of views to suffer greatly.

[1] http://www.pco.de/sensitive-cameras/pcopixelfly-usb/, verified 2015–05–03

The second camera is a commercially available Apogee Alta F32[2]. In contrast to the Pixelfly, its active cooling and higher quantum efficiency make the camera much more ideal when recording long exposure images of individual nanoparticles at low light conditions. However, its physical shutter and generally slow acquisition time make it very undesirable when mapping out the sample in order to locate interesting structures. Both cameras were controlled using their corresponding software provided by the manufacturers. However, the Apogee camera was also programmed to work with the open–source software μManager for automatic acquisition.

3.1.2 Limitations and drawbacks

No type of microscopy technique is without flaws. Much like their optical counterparts, the electrostatic lenses in the PEEM also suffer from both spherical and chromatic aberrations. In the case of electrons, spherical aberrations arise due to the electrostatic fields in the objective lens not being perfectly paraboloidal. This results in electron trajectories close to the edges of the lens being overcompensated, causing features in the images to look unfocused. While using a smaller contrast aperture reduces the amount of off–axis electrons by blocking out those that diverge too much, the total intensity will suffer and thus require much longer exposure times. Chromatic aberrations arise directly from the emitted photoelectrons having slightly different kinetic energies. Since the focal length of the electrostatic lenses is energy dependent, as the velocity of the electrons governs how long they are subjected to the electric field, there will be no well–defined point of focus [26].

Some further drawbacks include astigmatism and the simple fact that any charged particle will repel other particles of the same polarity. Astigmatism can have different causes, such as imperfections in the electrostatic lenses or stray magnetic fields interfering with the electrons. The result is often blurred or directionally distorted images, but astigmatism can be manually minimized by tuning the octupole stigmator. Coulomb interactions, also referred to as space charge effects in the PEEM, can essentially only be minimized by lowering the intensity of the photoemission signal, reducing the electrons' influence on one another. The presence of space charge effects can be seen by smaller objects appearing much bigger due to the electron cloud hitting a larger area on the

[2]http://www.ccd.com/alta_f32.html, verified 2015–05–03

MCP [26]. Finally, any instrument working in the nanoscale regime will be fundamentally dependent on a vibration–free environment. This is realized through a heavy, vibrationally damped optical table and by only running the ion pump to maintain the UHV in the main chamber.

3.1.3 Light sources

Throughout this project, all regions of interest were imaged using two different light sources. The first is a mercury discharge lamp and the second is a laser system capable of providing ultrashort light pulses. Both light sources have their separate strengths and weaknesses and will be described in short detail below.

Hg lamp

The mercury arc–discharge lamp was supplied by Focus GmbH, and consists of a transparent gas cell in which Hg atoms are excited by an applied voltage. This produces a very broad spectrum with a sharp peak at 4.9 eV [27], which is greater than the work function of any of the structures that were investigated. This allows for single photon photoemision, making it ideal for mapping out the samples.

Laser system

The Venteon CEP5[3] broadband oscillator belonged to the attosecond research group of Prof. Anne L'Huillier at the Division of Atomic Physics at Lund University. According to the manufacturer, it produces 2.75 nJ infrared pulses with durations as short as 5.5 fs centered around 800 nm (374.74 THz) at a repetition rate of 80 MHz. With temporally short pulses, they must instead have a broad energy distribution, as can be derived directly through Fourier's theorem since time is inversely proportional to frequency. The laser's spectrum in frequency domain is shown in fig. 3.2a), recorded using a spectrometer. Additionally, using the interferometric characterization technique known as a dispersion scan (d–scan) [28], one can also obtain the phase of the pulses, which then allows for a numerical reconstruction of the pulse in time–domain, as shown in fig. 3.2b).

[3] http://www.laserquantum.com/products/detail.cfm?id=75, verified 2015–05–03

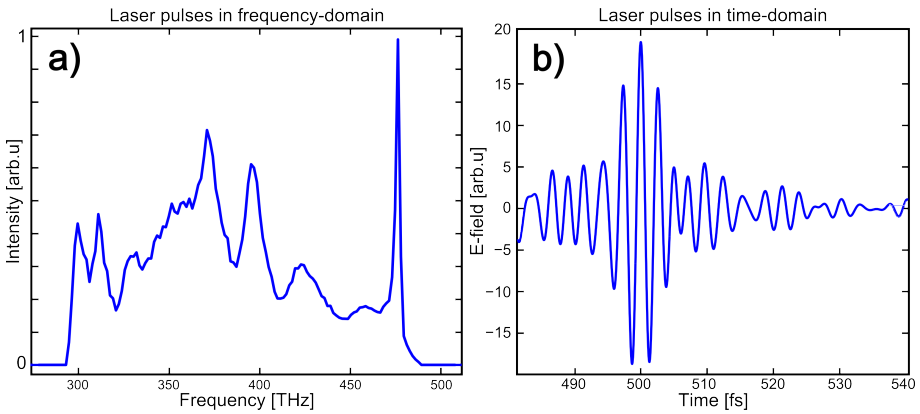

Figure 3.2: a) Frequency–domain spectrum of the pulses generated by the laser. b) Time–domain plot of the pulses generated by the laser.

As explained in section 3.1, incident light will hit the sample at a 25° angle with respect to the sample plane. This grazing incidence will result in the beam–profile on the sample being ellipsoidal. From observations, the spot size was estimated to be roughly 50 x 100 μm^2.

3.1.4 Samples

There are certain conditions which must the fulfilled for every sample to be imaged in a PEEM. First and foremost, the substrate of the sample must be conducting. As electrons are extracted from the nanostructures, a net charge will quickly build up unless the sample is grounded. Additionally, it is also crucial that the samples are properly mounted in their sample holders, as a tilted sample will result in an asymmetric field at the surface, giving rise to severe distortions which has to be compensated for each time the sample is moved. Ideally, scratches and similar features on the substrate should also be minimized, as they can give rise to an increased photoemission which in turn may greatly hamper imaging of the desired structures.

3.2 Optical setup

Independently of what type of measurement was performed, the laser was always sent through the interferometer, even if one of the two arms was occasionally blocked. Apart from not having to realign everything in–between experiments, this was also done in order to keep track of the light's dispersion, as all pulse characterization was carried out after all other optical elements. The IR–IR pump–probe setup can be built very robust as

a standard Michelson interferometer. Using a beam–splitter, half of the laser light was sent to a pair of mirrors while the other half was sent to another pair positioned on a translatable stage capable of changing the delay in a range of ±250 fs. By varying the relative path difference between the two arms, the recombined pulse is swept in time. The power of each arm was monitored on several occasions, and consistently a power ratio of 1:1 was measured, indicating that the interferometer was properly calibrated.

Perhaps the most important aspect for pump–probe experiments is to make sure that the pulse is temporally short enough, a property which is heavily influenced by dispersion from the various optical elements in the beam–path. Dispersion arises from the fact that different wavelengths propagate at different velocity through media. For glass or air, this results in the pulse being stretched in time, and is referred to as positive dispersion due to shorter wavelengths experiencing a higher refractive index in the material. In order to compensate for everything that the light has to propagate through, a pair of chirped mirrors is positioned in the beam path, reflecting different wavelengths at different depths of the material to effectively give a negative dispersion. Using a flip–mirror, the laser light can either be sent to the PEEM or to a separate station for d–scan characterization [28], without having to exchange any optical components. While performing d–scans allows for a minimization of the pulse–length through control of the total dispersion, it is important to keep in mind that the light must propagate through an identical amount of glass when going to the d–scan for characterization or the PEEM for measurements. This requires a second set of lenses and PEEM windows. A schematic overview of the optical setup used during the experiments is illustrated in fig. 3.3a). Finally, the light is focused onto the sample using a $f = 20$ cm achromat lens.

In conjunction with the d–scans, the current configuration of the PEEM also had windows on both sides of the sample, where light could enter at a 25° angle with respect to the sample plane. This allowed the metallic PEEM samples to be used as mirrors in order to directly visualize the beam–profile on the sample. Using a CCD camera, the light reflected off the sample was continuously monitored as the laser beam was swept across the sample. The shape of the beam–profile contained information about clusters or otherwise unwanted features on the sample surface, and the location of where the beam was hitting the CCD could be used to align the laser with respect to the field–of–view (FoV) of the PEEM.

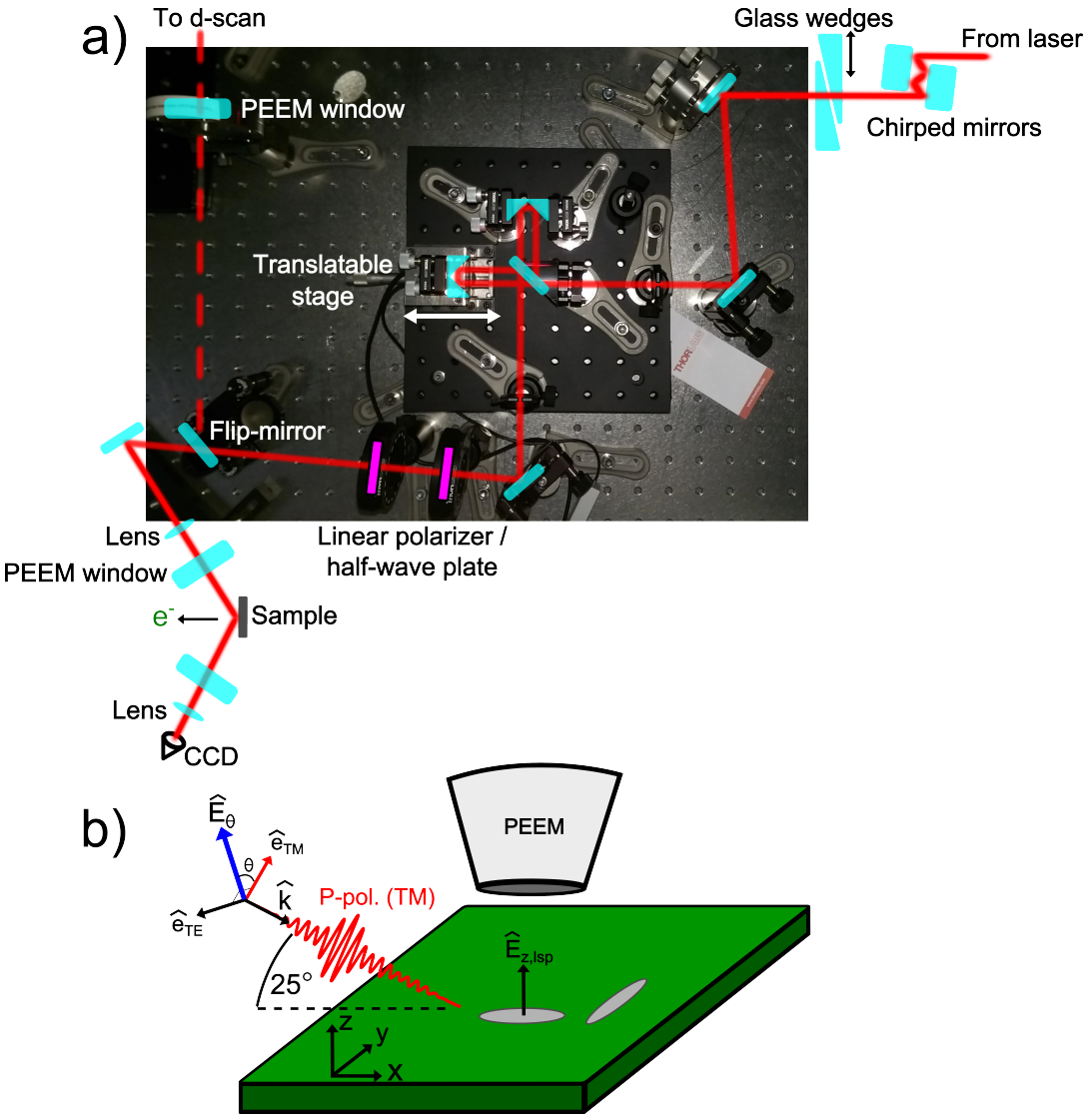

Figure 3.3: a) Schematic overview of the entire experimental setup as seen from above. b) Illustration of the most relevant angles for the excitation source / sample.

Additionally, the experimental setup allows for tuning of both the laser intensity and its polarization. This is achieved through a combination of a half–wave plate and a linear polarizer. A half–wave plate, or $\lambda/2$–plate, is an anisotropic crystal where polarized light will propagate at different velocity through the crystal depending on its polarization. Therefore, it introduces a phase shift to one of its two perpendicular vector components. As long as the incident light is linearly polarized, the outgoing light will also remain so. However, rotation of the half–wave plate will rotate the polarization by twice that angle, *i.e.* $\Delta\theta_{\text{pol}} = 2\Delta\theta_{\lambda/2}$. An ideal linear polarizer only transmits light whose electric field vector component is aligned parallel to the axis of the polarizer. Both the half–wave plate and the linear polarizers used throughout this project were broadband to cover the entire spectral range of the laser pulses.

Depending on in which order the half–wave plate and the linear polarizer are positioned in the experimental setup, different outcomes are achieved. In the first configuration, the half–wave plate is followed by the linear polarizer. This allows for tuning of the intensity of the laser light in a reversible way. As the polarization of the light is shifted away from the maximum throughput angle of the linear polarizer by rotation of the half–wave plate, less light will be transmitted. In the second configuration, the linear polarizer is followed by the half–wave plate which is then rotated. This allows for a simple and straightforward way to freely rotate the polarization of the transmitted light while maintaining the same intensity.

A very important aspect of polarization dependent measurements is keeping track of the polarization of the light with respect to the sample plane. When the electric field component oscillates in the same plane as the sample, the light is considered S–polarized (or transverse electric, $\vec{e}_{TE}$). Similarly, with the electric field component oscillating in the plane of incidence, it is considered P–polarized (or transverse magnetic, $\vec{e}_{TM}$). A schematic representation of the most important angles in the experimental setup is shown in 3.3b).

Autocorrelation tracing

For a Michelson interferometer, the electric field $\vec{E}(t,\tau)$ of the recombined pulse is given by

$$\vec{E}(t,\tau) = \vec{E}(t) + \vec{E}(t-\tau) \tag{3.1}$$

where $\vec{E}(t)$ is the response from one arm and $\vec{E}(t-\tau)$ is the delayed response from the other arm. From equations 2.7 and 3.1, the integrated photoemission yield $Y(\vec{r},\tau)$, as the delay between the two arms τ is swept in time is then given by

$$Y(\vec{r},\tau) \propto \int_{-\infty}^{\infty} |\vec{E}(\vec{r},t) + \vec{E}(\vec{r},t-\tau)|^{2n} \mathrm{d}t \tag{3.2}$$

where $\vec{E}(\vec{r},t)$ is the near–field response induced by one of the laser pulses and n is the expected order of photoemission. In contrast to many spectroscopic methods, an autocorrelation trace retains the phase information of the response, and can thus be used to investigate plasmonic near–fields in real–time.

3.3 Image processing

For the type of imaging experiments carried out in this project, numerous things can go wrong, many of which are very hard to actively prevent. However, depending on the severity of the issue, much can be accounted for via post–processing of the data while still retaining all relevant information. The most consistent encounters were artifacts on the CCD (hot pixels) and drift in the PEEM.

Hot pixels were selectively removed, as they could easily be identified by single, saturated pixels in the images. Drift in an image series can be accounted for by selecting a fixed point, preferably at a structure which have a strong enough photoemission signal to be traced throughout the entire image series. Each image is then shifted linearly so that the structure match up with the first fixed point. After compensating for the various inconsistencies, a Gaussian blur filter was employed to each image to weight every pixel against its immediate neighbors. Additionally, a mean background value taken from a region without any measurable photoemission signal was then subtracted from each individual image.

3.4 FDTD simulation setup

Throughout this project, two separate FDTD simulation softwares were thoroughly tested. Because this was the first time such software was used, a careful evaluation of their functionalities was performed. The evaluation was based on a series of features that were desired to properly correlate simulations with PEEM experiments. This included dielectric databases covering the investigated materials, support for customized excitation sources at arbitrary angles, straightforward ways to collect E–fields at desired points in space as well as the option to collect the absorption cross–section spectra. Additionally, the validity of the simulations were confirmed by, amongst other things, recreating previously published and acknowledged studies resembling the current work [25]. For all simulations presented in this project, the commercially available software FDTD Solutions by Lumerical Inc.[4] was used.

The dielectric function used to represent silver was obtained using a Drude model based on sampled data by Palik [29]. The fitting parameters were chosen to cover the range 550–1100 nm (300–550 THz), as shown in fig. 3.4a–b), in order to sufficiently match the spectral bandwidth of the laser pulses. The presence of a substrate was modeled using a standard SiO_2 glass slab which deliberately extended outside the PML boundaries, which in turn negated any potential issues due to discontinuities at the edges of the simulation volume.

In order to simulate the experimental conditions, the incident excitation pulse was injected through a box enclosing the nanoparticle using the total–field scattered–field formulation at a 25° angle with respect to the sample plane. The excitation pulse itself was modeled to resemble the actual pulses generated by the laser system in both time– and frequency–domain. This resulted in a dampened cosinusoid, 5.5 fs long primary peak centered around 800 nm, with 3 additional smaller satellites, as shown in fig. 3.4c). To prevent scattered fields reflecting back from the outer boundaries of the simulation volume, at least 16 layers of PML was used.

Due to computational memory constraints, the staircase mesh grid size surrounding the nanoparticle was chosen with a minimum element size of 2.5 nm. However, convergence testing was carried out to make sure that the fields close to the edges of the structure were well resolved at this grid size. Note that rounding of the corners of the cube was not

[4] https://www.lumerical.com/tcad-products/fdtd/, verified 2015–05–03

considered in the simulations.

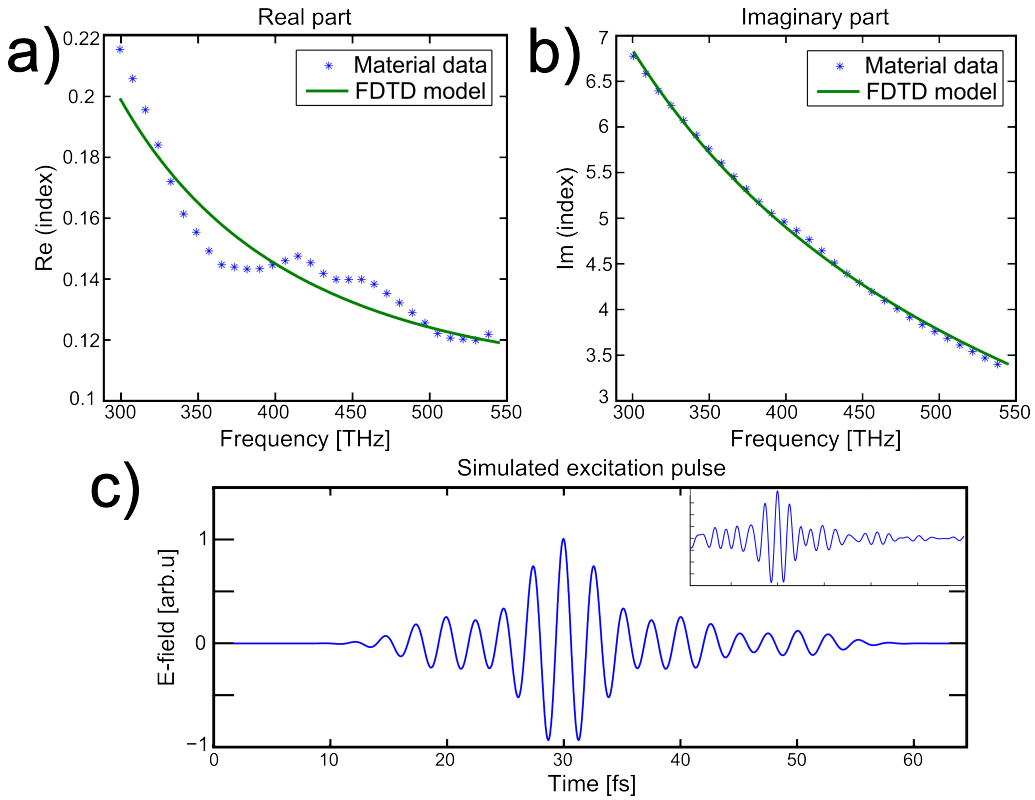

Figure 3.4: a) Real part of the Ag dielectric function, with both experimental data and fit. b) Imaginary part of the Ag dielectric function. c) Excitation pulse. Inset: time–domain plot of the pulses generated by the actual laser system.

Chapter 4

Results and discussion

In this chapter, the major results achieved during the course of this project will be presented. This is further divided into two main sections, each focusing solely on only one type of nanostructure. They will include both PEEM measurements and complementary FDTD simulations, followed by a more in–depth analysis of the results. The general outline consists of investigating the photoemission (PE) yield of the plasmonic response under different circumstances.

4.1 Sample preparation

Throughout this project, several different samples were studied, including various semiconducting nanowires, a few different silver nanostructures, and gold bowties. Among these, some of the silver nanostructures proved to be particularly interesting and will thus be the focus for the remainder of this thesis. The structures in question are cubes and ellipsoids resembling grains of rice.

Both the Ag nanocube and nanoellipsoid structures were grown by Hongxing Xu's group at the Department of Physics of the Chinese Academy of Science in Beijing using a polyol–synthesis technique [30]. Through careful control of the growth conditions, such as temperature and pressure, growth along specific crystal facets can be encouraged. As a result, the nanocubes are bounded almost entirely by {100} facets. The nanoellipsoids, however, have a more complicated stacking sequence, although FCC(111) facets have been shown to make up most of the crystal surface. Initially dispersed in ethanol, the structures were deposited onto substrates consisting of borosilicate glass Schott BK7 with a 150 nm

thick indium tin oxide (ITO) layer by completely wetting the surface. Excess solution was then gently blown away using a stream of air. A rough inspection of the sample was carried out using an optical microscope. This allows one to judge how tilted the samples are, as the focus should not vary significantly between two opposite ends of the sample holder. The samples were then immediately transferred into the PEEM UHV system to minimize exposure to air. Fig. 4.1 shows the said structures, imaged using a scanning electron microscope (SEM).

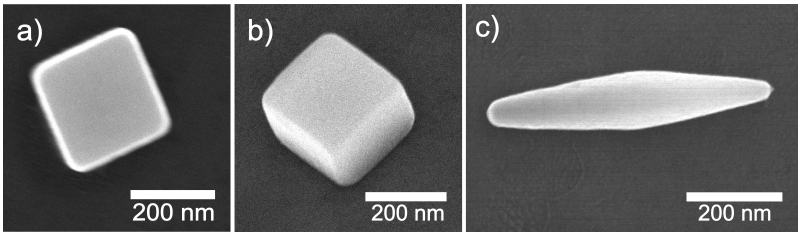

Figure 4.1: a) SEM image of a Ag nanocube. b) Tilted SEM image of a Ag nanocube, revealing that they are lying with a facet flat on the substrate, and not submerged into it. c) SEM image of a Ag nanoellipsoid. The magnification of all images presented in this report is indicated by a scale bar which is manually added via post–processing.

4.2 Ag nanocubes

The use of both light sources described in section 3.1.3 was in the present case a necessity. When illuminating silver structures on an ITO substrate with the laser, the photoemission yield from the substrate will be many orders of magnitude lower than that from the structures, almost indistinguishable from the noise floor. On the other hand, when illuminating the sample with the Hg lamp, clear images of both the substrate and deposited nanostructures could be recorded in a fairly large field of view (≥ 76 μm) at as low exposure times as 100 ms. This allowed for a quick and easy way of mapping out the sample in order to locate suitable structures for further investigation. Once an interesting region had been located, the laser beam was sent into the PEEM chamber. While monitoring the laser light reflected off the sample as described in section 3.2, the laser beam was systematically swept across the sample until photoemission was detected in the PEEM. With the laser beam overlapping with the center of the field–of–view (FoV) of the PEEM, different types of measurements can be carried out. Overall, the Ag nanocubes were extremely well–defined, with essentially every observed cube having sides of 250 ± 10 nm. This geometry was deliberately chosen as the cubes were designed to exhibit plasmon resonances within the spectral bandwidth of the laser.

4.2.1 IR PEEM experiments

In the first part of this section, a power law measurement is presented in order to argue what order of multiphoton photoemission (MPPE) is governing the measured signal. In the second part, the dependence of the PE yield on incident laser light polarization is investigated.

Determining the order of multiphoton photoemission

In fig. 4.2a–b), a collection of individual nanocubes can be seen within a single 10 μm FoV, recorded using only the Hg lamp and only the laser, respectively. Additionally, a corresponding SEM image of the same area is shown in fig. 4.2c). For all laser–PEEM images presented in this report, the excitation light is incident from the right. In measuring the MPPE yield as a function of laser intensity, the order of the photoemission process can be determined. More specifically, the yield depends the local intensity raised to the power of n, where n is the minimum number of incident photons required to surpass the work function threshold of the material. If an n–photon photoemission process dominates the signal, a linear regression of the plot $\log I_{\mathrm{MPPE}}$ vs. $\log I_{\mathrm{laser}}$ should then be a straight line with slope n.

While varying the laser power using the half–wave plate, as described in section 3.2, the laser power was measured and an image was recorded for each increment. The integrated response at each increment for different individual nanocubes, identified by a corresponding colored square, can be seen in fig. 4.2d). In the same plot, a linear regression of each set of data points is shown, whose slope corresponds to the order of multiphoton photoemission. Similarly, the averaged signal from all cubes and its linear regression can be seen in fig. 4.2e). In order to increase stability during the power law measurement, only one arm of the interferometer was used and the photoemission signal was maximized through the use of a big contrast aperture.

From the cubes presented in the power–law measurement shown in fig. 4.2, it is clear that a strong tendency for three–photon photoemission is present. This is also in agreement with previous studies, where the work function for Ag(100) has been determined to be $\phi_{\mathrm{Ag(100)}} = 4.22 \pm 0.04$ eV through photoemission experiments [31]. Considering an estimated central photon energy of the laser of 1.55 eV, then at least 3 photons are required to exceed the work function.

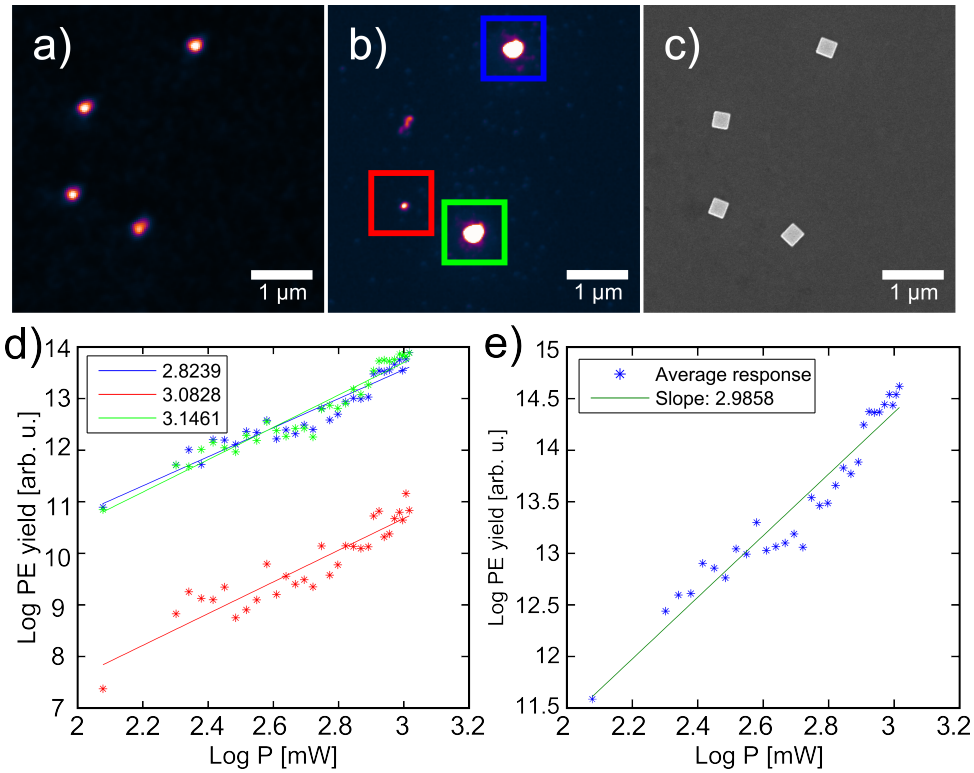

Figure 4.2: a) Hg lamp image of an ensemble of nanocubes. b) Laser light image. c) SEM image. d) Individual power–law plots, where each color corresponds to a separate cube. Note that the fourth cube was not considered due to heavy irregularities in its photoemission. e) Averaged power–law plot of all considered cubes.

While some sources for error may still remain, such as thermal effects due to heating of the sample, this contribution was deemed low enough not to influence the emission significantly. Thus, only three–photon photoemission for the nanocubes will be considered henceforth.

Polarization dependence

The polarization dependence on the photoemission yield was investigated by gradually rotating the polarization of the incident laser light using the half–wave plate according to the description in section 3.2. The half–wave plate was rotated from 0° to 360° in steps of 5° and an image was recorded at each increment. Note that this would correspond to a 720° rotation of the polarization, since $\Delta\theta_{\text{pol}} = 2\Delta\theta_{\lambda/2}$. Both arms of the interferometer were used during the measurement, with the delay stage positioned at the maximum temporal overlap. Unfortunately, at the time these measurements were carried out, the half–wave plate was not properly aligned in its mount, but 4° off, corresponding to a polarization 8° off from its intended orientation. Due to this, no images in the sweeps were recorded

using completely 'pure' S– or P–polarized light (minimum 2° off).

In fig. 4.3a), two individual nanocubes rotated roughly 45° with respect to each other can be seen within a single 6 μm FoV, recorded using only the Hg lamp. After drift–compensation, the entire polarization series summed up is shown in fig. 4.3b). Additionally, a corresponding SEM image of the same area is shown in fig. 4.3c). Fig. 4.3d–g) show the recorded photoemission response from the bottom cube for a few different polarizations. Similarly, fig. 4.3h–k) show the recorded photoemission response from the top cube. For simplicity, these cubes will henceforth be referred to as the 'angled' and 'normal' cube, respectively.

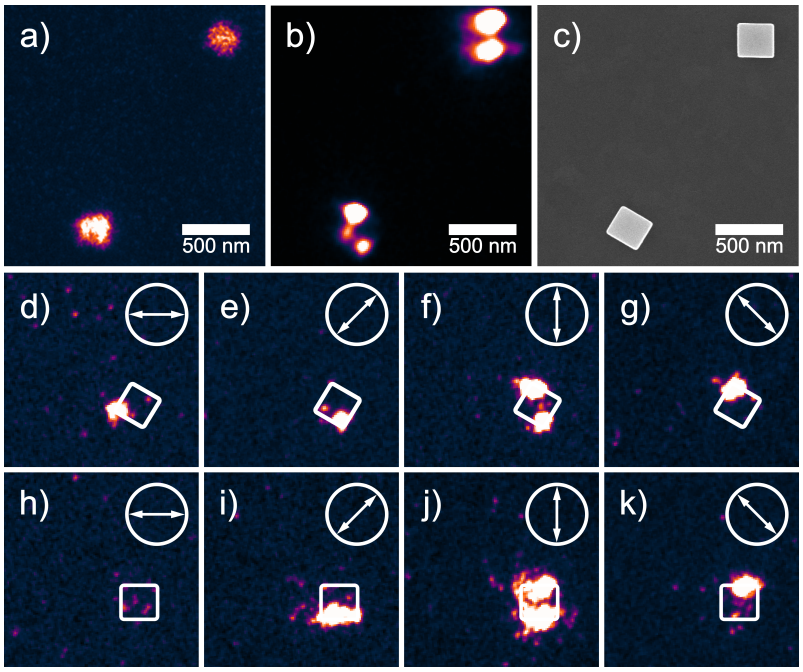

Figure 4.3: a) Hg lamp image. b) Summed polarization sweep. c) SEM image. d–g) PEEM images of the angled cube for different polarizations. The edges of the cube has been outlined for clarification and the polarization angle with respect to the wavefronts of the light is indicated by the arrows. h–k) PEEM images of the normal cube for different polarizations.

4.2.2 FDTD simulations

To facilitate analysis of the measured data, FDTD simulations modeled after the experimental setup were carried out. For this purpose, an individual silver nanocube with 250 nm sides sitting in contact with a substrate was constructed. The structure, as seen from two different angles, is shown in fig. 4.4. The arrows indicate the incident angle and polarization of the excitation source. For all FDTD simulation images presented in this

report, the excitation light is incident from the right. The same excitation pulse settings, dielectric function fitting, as well as mesh grid size that were described in section 3.4 were used for all nanocube simulations.

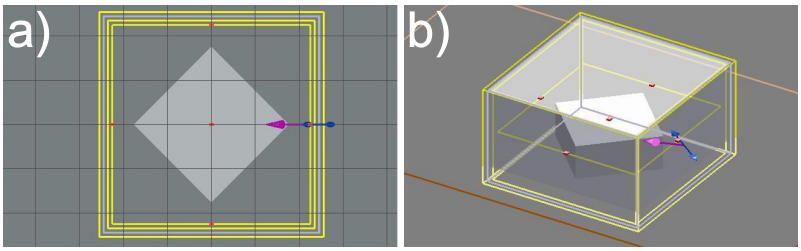

Figure 4.4: a–b) Ag nanocube as seen from a few different angles. The arrows indicate incident angle and polarization of the excitation source.

The electric field components were sampled 3 nm above the top facet of the nanocube in a plane parallel to the sample plane. Fig. 4.5a–b) show FDTD simulations of the z–component of the E–fields from a Ag nanocube resembling the 'angled' cube at two different time steps, excited using S– and P–polarized light, respectively. It is also possible to estimate what a PEEM image could look like based on the simulated electromagnetic response. Thus, evaluating equation 2.7 with $n = 3$ at each point in space, again for both S– and P–polarized light, results in the images shown in fig. 4.5c–d). The same procedure is then repeated for another Ag nanocube rotated 45° with respect to the first, as shown in 4.5e–h). The numerical values indicated in the colorbars show the maximum E–field enhancement relative to the amplitude of the excitation pulse.

A complete polarization scan was also simulated using FDTD Solutions. Since Maxwell's equations are linear, one could describe the electromagnetic field response $\vec{E}(\vec{r}, t)$ for a system excited by a source with a certain polarization θ as

$$\vec{E}_\theta(\vec{r}, t) = \vec{E}_S(\vec{r}, t) \sin\theta + \vec{E}_P(\vec{r}, t) \cos\theta \tag{4.1}$$

where $\vec{E}_S(\vec{r}, t)$ and $\vec{E}_P(\vec{r}, t)$ are the responses for pure S– and P–polarized excitation, respectively. Relations are chosen based on the angles shown in fig. 3.3b), *i.e.* 0° represent P–polarized excitation. Recalling equation 2.7, the total PE yield can then be calculated as

$$Y_\theta(\vec{r}) \propto \int_{-\infty}^{\infty} |\vec{E}_S(\vec{r}, t) \sin\theta + \vec{E}_P(\vec{r}, t) \cos\theta|^{2n} \mathrm{d}t \tag{4.2}$$

where n is the expected order of MPPE. Thus, by merely running two separate simulations,

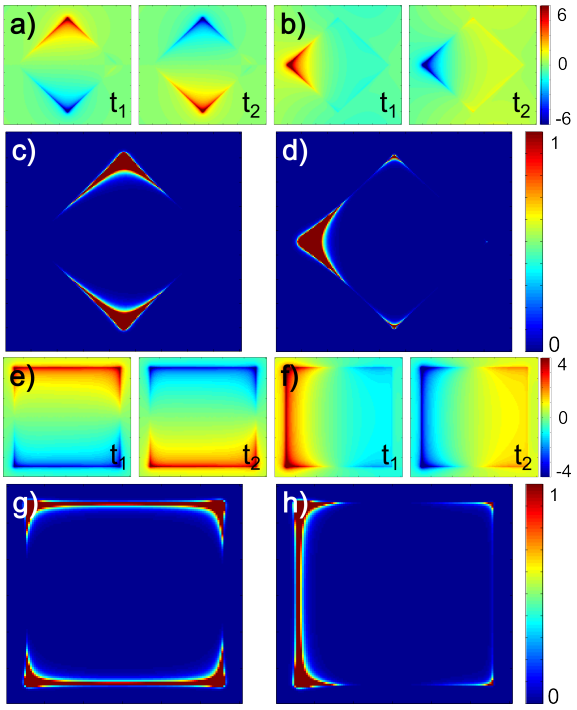

Figure 4.5: a) Simulated near–field distribution at two arbitrary time–steps for the angled cube using S–polarized excitation. b) Using P–polarized excitation. c) Simulated PEEM image for the angled cube for S–polarized excitation, normalized to 1. d) For P–polarized excitation. e–h) Same procedure, but for the normal cube.

using S– and P–polarization, a complete polarization sweep much like the measurements could be simulated. Fig. 4.6a,c) show the entire polarization sweep summed up for both the PEEM measurement and the simulation by evaluating equation 4.2, only considering the z–component of the E–fields. Additionally, summing the PE yield from the different corners for both sets of data and plotting them as a function of polarization angle results in the plots shown in fig. 4.6b,d). To increase the signal–to–noise ratio, the first half of the polarization sweep (spanning 2π in total) was added onto the second half. Additionally, the misalignment of the half–wave plate was accounted for by shifting all data points $+8°$ in the plot. For the normal cube, the entire length of the cube was considered instead. The reasoning for this is that the PE yield could not properly be distinguished from specific corners.

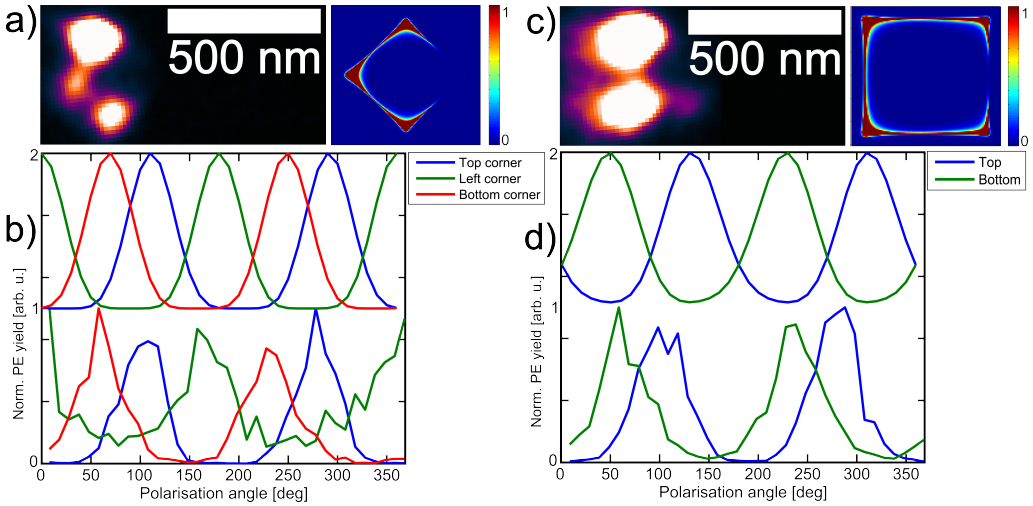

Figure 4.6: a) Measured and simulated polarization sweep for the angled cube. b) Summed PE yield for the various corners as a function of polarization angle for both simulations (top) and experiments (bottom). c) Measured and simulated polarization sweep for the normal cube. d) Summed PE yield for the entire length of the cube as a function of polarization angle for both simulations (top) and experiments (bottom).

4.2.3 Correlating PEEM measurements with simulations

In order to draw any conclusions regarding the polarization dependence of the MPPE, one must know where on the surface of the nanostructures the PE yield is maximized. From fig. 4.3b), showing the sum of the entire polarization series, it is evident that maximum photoemission is obtained from the corners of the cube, much like the simulated PEEM images show for S– and P–polarization, respectively, as is shown in fig. 4.5c–d). This is also in agreement with several previous studies [32–34]. The increased yield in photoemission signal from the corners originates from accumulation of charges there. Therefore, one can expect the yield to reach peak values when the excitation polarization is aligned with the diagonals of the nanocube compared to parallel to its sides. [35] This is also consistent with the FDTD simulations shown in fig. 4.5a–b,e–f), where the maximum local field enhancement is greater for the cube whose corners are aligned with the polarization of the light.

From the plots shown in fig. 4.6b,d), the simulated polarization sweep fits remarkably well with the measured data. This agreement indicates that the assumptions regarding the linearity of the electromagnetic response for different polarizations are reasonable. The fact that the simulated polarization sweep initially only considered pure S– and P–polarized excitation indicates that as soon as the polarization of the light deviates from any of these, a coherent superposition of modes caused by both polarizations is excited in

the structure. In order to present a qualitative description of the PE yield polarization dependence, the most prominent modes that can be excited in a nanocube must first be discussed.

To get an idea of what a surface plasmon mode looks like in a nanocube, consider a cube with 250 nm sides suspended in vacuum, excited by a normal incidence light pulse with a spectral range corresponding to the laser pulses used during the PEEM experiments. At normal incidence, only one type of polarization of the light needs to be considered due to symmetry. Under these circumstances, the absorption cross–section plots for both the angled and normal cubes are shown in fig. 4.7a–b). Data to calculate the absorption cross–section were recorded just inside the box from where the excitation pulse is injected. From the absorption cross–sections, which appears qualitatively very similar, there is only one clear peak associated with the near–field for both cubes. The corresponding steady–state field distributions for the two cubes are shown in fig. 4.7c–d) for both the top and bottom facet of each cube. These were obtained through a Discrete Fourier Transform (DFT) of the z–component of the E–fields at 458 THz. Based on this, a 3D representation of the charge distributions on the surfaces of the cubes are shown in the same figure. In fig. 4.7c–d), the charge distribution of the two modes reside on either side of the cube, resulting in a large electric dipole moment that couples strongly to light. These will henceforth be referred to as the bright dipolar modes. For the sake of clarification, an example of what a dark quadrupolar mode could look like for the normal cube is shown in fig. 4.7e).

Since the MPPE signal measured in the PEEM is almost exclusively originating from electrons being emitted normal to the structure surface, it is therefore reasonable to only consider the top facet of the nanocube. Let us now move on to the case when the light is incident at a grazing angle. Absorption cross–section plots for both cubes and both S– and P–polarized excitation is shown in fig. 4.8 and fig. 4.9, respectively. Compared to the absorption cross–sections at normal incidence, additional peaks emerge in the spectrum for both cubes. However, due to the high non–linearity of the MPPE process, some assumptions can be made. Since the intensity of 3–photon photoemission is proportional to the electric field to the power of 6, should one resonance be twice as strong as another, then the total PE yield would be 2^6 times as large for the former resonance. Thus, for the angled cube, the peak which is partly present at 545 THz can be assumed to completely dominate the response for both polarizations. For the normal cube, however,

the difference in magnitude between the two absorption peaks for S–polarized light is too small, and thus both resonances must be considered. Steady–state field distributions for all absorption peaks are shown in their respective figures.

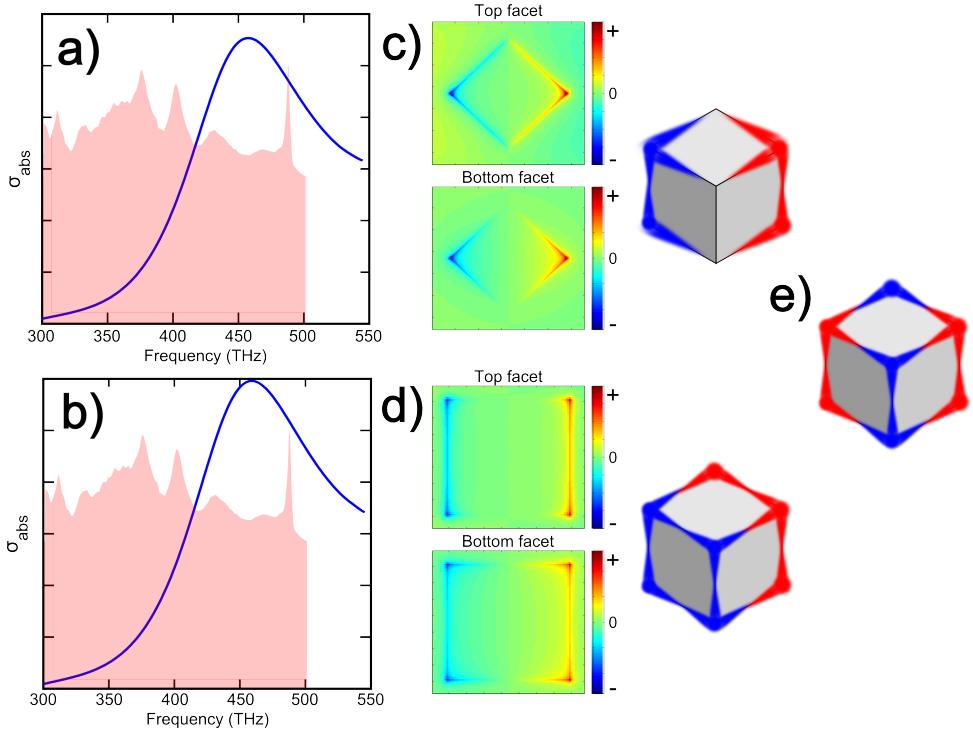

Figure 4.7: a) Absorption cross–section for the angled cube. The red shaded area indicates the approximate spectral window of the laser. b) Absorption cross–section for the normal cube. c–d) Charge distribution for each cube corresponding to the peak at 458 THz along with a 3D representation. e) 3D representation of a dark quadrupolar mode.

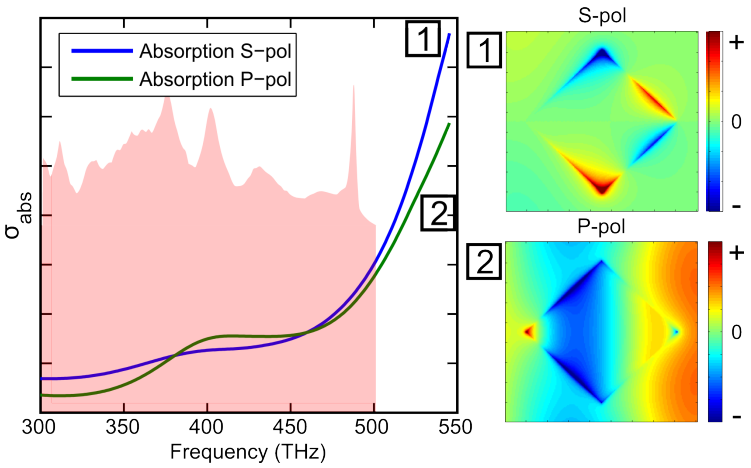

Figure 4.8: Absorption cross–section for the angled cube for both S- and P-polarized excitation. The red shaded area indicates the approximate spectral window of the laser. 1–2) E_z steady–state field distributions for the peaks marked 1 and 2, evaluated at 545 THz.

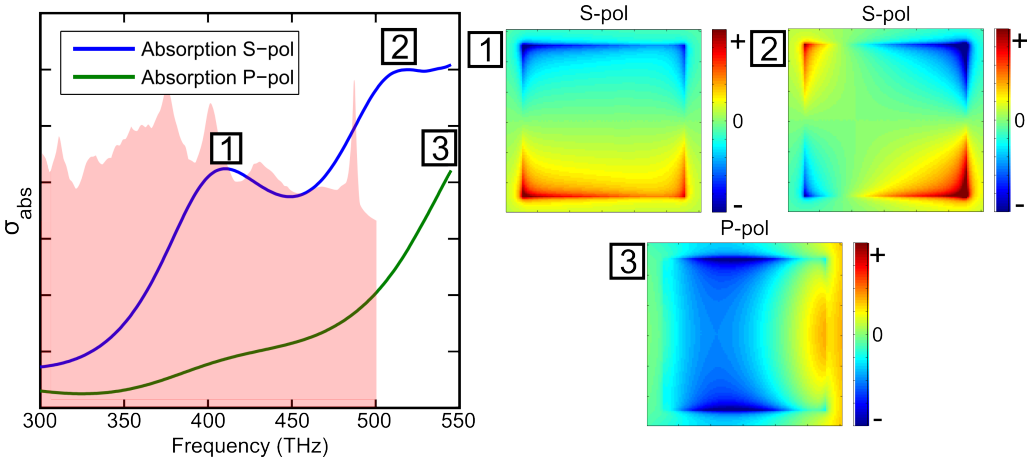

Figure 4.9: Absorption cross–section for the normal cube for both S- and P-polarized excitation. The red shaded area indicates the approximate spectral window of the laser. 1–3) E_z steady–state field distributions for the peaks marked 1 through 3, evaluated at 409, 516 and 545 THz, respectively.

For the angled cube, both the dipolar (fig. 4.7c)) and quadrupolar (fig. 4.8) modes have, as previously discussed, maximum charge distribution at the corners of the cube, resulting in the observed MPPE only from the corners. Additionally, for P–polarized excitation no photoemission was ever observed from the corner that first gets struck by the light. However, this is in accordance with similar previous studies [36]. For the normal cube, no MPPE was observed from any of its sides when excited with P–polarized light. Also, as a first approach, only the dipolar mode will be considered for the normal cube at S–polarized excitation. Taking this into consideration along with the modes presented in fig. 4.8 and fig. 4.9, a simple table of possible combinations is shown in fig. 4.10.

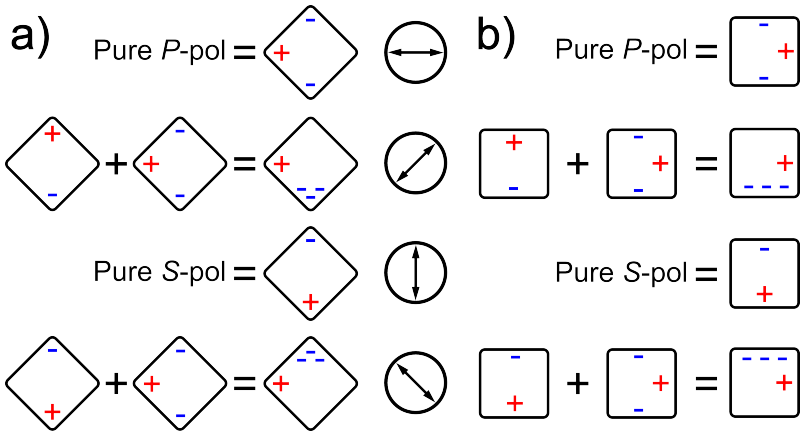

Figure 4.10: Superposition table of the different mode combinations resulting in the local field enhancements being focused in specific corners of the cube for a) the angled cube and b) the normal cube. Polarization angle with respect to the wavefronts of the light is indicated by the arrows.

Looking at fig. 4.3 and fig. 4.6 based on the table of combinations shown in fig. 4.10, this approach is sufficient to qualitatively describe the behavior of the angled cube. For the normal cube, however, additional effects must be considered due to the grazing incidence of the light, as can be seen from the quadrupolar mode in fig. 4.9[2]. In the steady–state field distribution, the quadrupolar mode has an accumulation of charges in the corners that first get struck by the excitation source. This will result in a different superposition of modes in these regions. When summing up the simulated polarization sweep, if one instead of the entire length of the sides only considers the PE yield from the corners where the greatest accumulation of charges is expected, then the yield as a function of polarization angle as shown in fig. 4.11 is obtained.

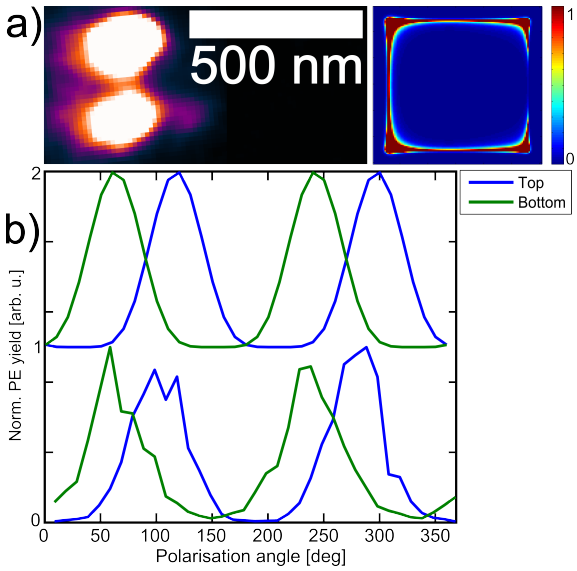

Figure 4.11: a) Measured and simulated polarization sweep for the normal cube. b) (Top) Summed PE yield for the corners that first gets struck by the excitation light (rightmost) as a function of polarization angle. (Bottom) Summed PE yield as a function of polarization angle for the PEEM measurement.

Essentially, by simply tuning the polarization of an incident excitation source, a superposition of symmetric and antisymmetric modes will induce a strong enhancement of the near–field in specific corners of a nanocube, while at the same time canceling the near–fields in other corners. This polarization dependence is qualitatively yet accurately explained through a simple system of superpositions of modes excited by S– and P–polarized light.

However, this model does not take into account the symmetry–breaking presence of a substrate which will induce a hybridization of modes in the nanocube [34,37]. Nonetheless, these factors are outside the scope of this work and will thus not be discussed further.

Links between LSP response and cube corner radii for smaller silver nanocubes (100–

150 nm sides) have also been investigated [35, 38]. Apart from trends showing that cubes with sharper corners being more influenced by their orientation relative to the polarization of the excitation source, no further correlations were found. While no similar investigation has been carried out in the present work, the cube corner radius compared to the relative size of the cube was believed to be small enough not to cause any significantly different behavior.

4.3 Ag nanoellipsoids

The second type of nanostructure featured in this project report is the Ag nanoellipsoids. The same procedure as was described in section 4.2.1 was followed to locate interesting regions. However, as will be shown in the following sections, the MPPE yield from the nanoellipsoids also varied significantly with structure orientation, further complicating the task of locating interesting structures using only the laser. Also, some effort had to be made in order to distinguish between single grains and clusters/disfigured structures due to the limited spatial resolution of the PEEM. Unfortunately, this could only be confirmed via post–inspection in a SEM. That said, the studied Ag nanograins were overall well–defined and typically 300–600 nm long and 90–110 nm thick. This geometry was deliberately chosen as the grains were designed to exhibit plasmon resonances within the spectral bandwidth of the laser.

4.3.1 IR PEEM experiments

In the first part of this section, a power law measurement is presented in order to argue what order of multiphoton photoemission is governing the measured signal. In the second part, the dependence of the LSPRs on incident laser polarization is investigated. In the third part, the temporal near–field dynamics of the LSPRs is investigated through IR–IR pump–probe measurements.

Determining the order of photoemission

In fig. 4.12a–b), a total of three separate nanograins have been recorded in a 3 and 5 μm FoV, respectively. For the grain shown in fig. 4.12a), MPPE is observed from both separate ends of the same grain simultaneously. The same procedure as was described in section 4.2.1 was followed to record a power–law measurement.

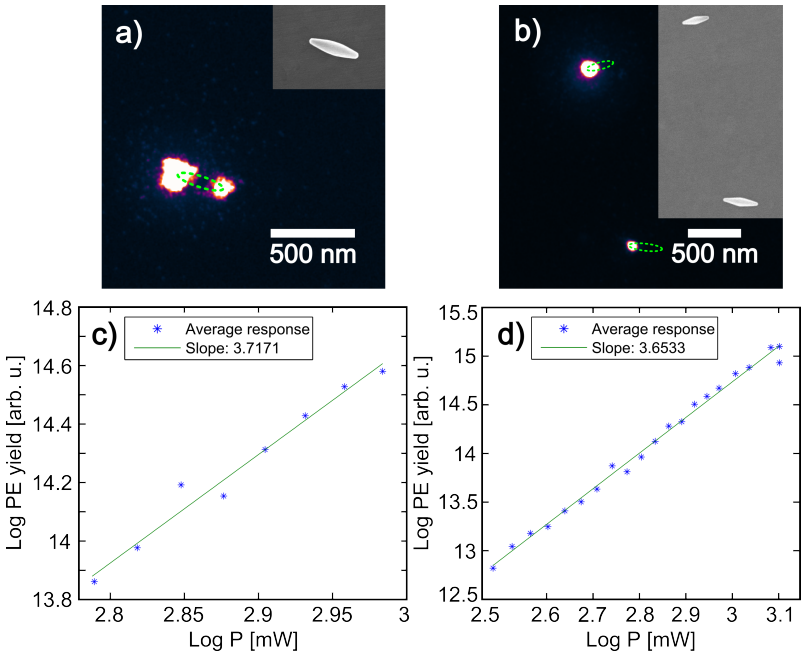

Figure 4.12: a–b) Three individual nanograins imaged with the laser. The grains have been outlined for clarification. Insets: SEM images of each grain. c) Averaged power–law plot for both spots of the same grain. d) Averaged power–law plot for the two grains.

From the plots presented in fig. 4.12c–d), there is a tendency towards either three– or four–photon photoemission. While the trend towards three–photon photoemission is not as clear as for the nanocubes, the additional higher–order contribution can be attributed to *e.g.* the surface of the ellipsoids not being bound entirely by the same type of crystal facets. After comparison with simulations considering both 3 and 4 photon photoemission, the best correlation with experiments was found for a 3 photon process, which is also in agreement with other studies [36]. Additionally, the work function for Ag(111) has been determined to be $\phi_{\mathrm{Ag(111)}} = 4.46 \pm 0.02$ eV [31]. Considering an estimated central photon energy of the laser of 1.55 eV (800 nm), then at least 3 photons are required to exceed the work function threshold. For simplicity, only three–photon photoemission for the nanograins will be considered henceforth.

Polarization investigation

The polarization dependence of the PE yield was investigated by comparing different silver nanograins rotated some angle ($> 45°$) with respect to each other. In fig. 4.13a), two such grains can be seen within a single FoV imaged with the Hg lamp. Fig. 4.13b) shows the same system imaged using both the Hg lamp and P–polarized laser light simultaneously, while fig. 4.13c–d) were recorded when exciting the structures using only P– or S–polarized

light, respectively. Here, it is worth noting that the image recorded using S–polarized light had significantly higher intensity of the incoming light. Finally, a SEM image of the same grains is shown in fig. 4.13e).

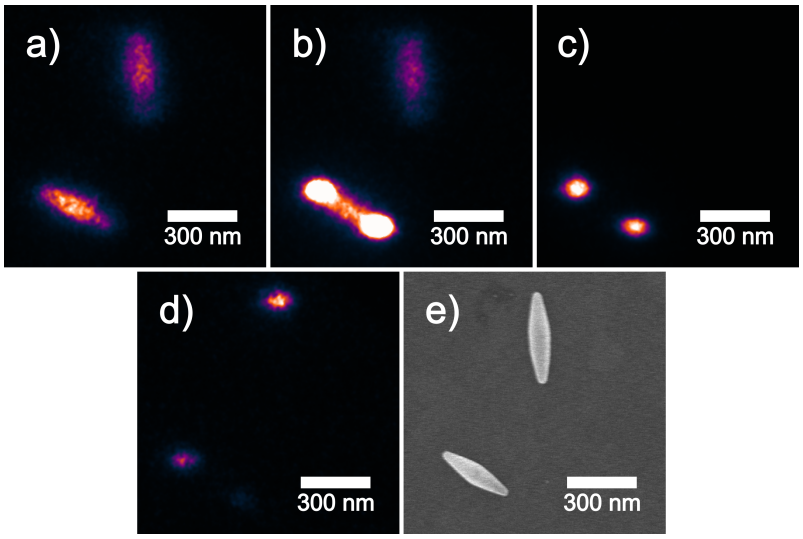

Figure 4.13: a) Hg lamp image. b) Hg lamp + P–polarized IR image. c) P–polarized IR image. d) S–polarized IR image. e) SEM image.

For the grains presented in fig. 4.13, there is a strong polarization dependence for the orientation of the structures and observed MPPE yield. This is well in accordance with theory, and as was explained in section 2.2.2, this behavior can be attributed to the excitation of bright and dark modes. As will be shown through FDTD simulations in fig. 4.16, the even quadrupolar mode ($m = 2$) will be the most dominant mode for all nanograin lengths considered. However, because of symmetry, the quadrupolar mode is forbidden for structures excited at normal incidence.

One could then argue that the dipolar ($m = 1$) or octupolar mode ($m = 3$), which are also present within the spectral window of the laser for certain nanograin lengths, should show up in the PEEM for nanograins oriented vertically in the sample plane when excited by S–polarized light. However, another important factor to consider is that for this orientation, the electric field vector of the light will be almost perpendicular to the normal component of the sample surface due to the grazing incidence of the light, as illustrated in fig. 3.3b). As a result, the light will couple poorly to the z–component of the near–fields, effectively reducing the MPPE yield. Because of these two reasons, grains oriented vertically in the sample plane were essentially invisible when illuminating with the laser.

On the other hand, for P–polarized excitation of grains oriented horizontally in the sample plane, MPPE could be observed from one or both ends of the grain. Much in the same way the nanocubes behaved, the maximum field enhancement is locally confined to the two ends of the grain, resulting in a very strong coupling to the light in these regions. For grains oriented perpendicular to the electric field component of the incident light, no longitudinal modes will be excited whatsoever, and the transverse modes are usually only found in the UV regions.

IR–IR Pump–probe delay sweeps

Unlike the nanocubes, the resolution along with the MPPE yield from nanograins was high enough to allow the two ends to be individually distinguished when excited with P–polarized light. This made them ideal systems for pump–probe measurements.

Fig. 4.14a) shows a roughly 550 nm long grain imaged using P–polarized laser light at maximum temporal overlap between the two arms of the interferometer. While the intensity ratio between the two ends of a grain varied greatly, it was always the end farthest from the excitation source that gave maximum MPPE signal. This observation is nonetheless in accordance with previous similar studies [36, 39]. For simplicity, the end of the nanograin which first gets struck by the incident light will henceforth be referred to as the 'close end', while the opposite end will be referred to as the 'far end'.

While stepwise sweeping the delay τ between the two arms of the interferometer, an image was recorded for each increment. This was typically done in a range corresponding to ± 25 fs from the central overlap. According to equation 3.2, the PE yield in the image series will then be a local autocorrelation of the near–field induced by a laser pulse. The near–field autocorrelation traces from the two ends of the grain are shown in fig. 4.14b), obtained by integrating the local PE yield from each end for each delay between the pump and probe pulses. Already at a delay of 5 fs, a slight shift towards longer delays can be seen in the autocorrelation trace for the far end. The measurement was then repeated using a smaller time–step, centered around the region where the greatest shifts emerged. A closer look at the shift is shown in fig. 4.14c).

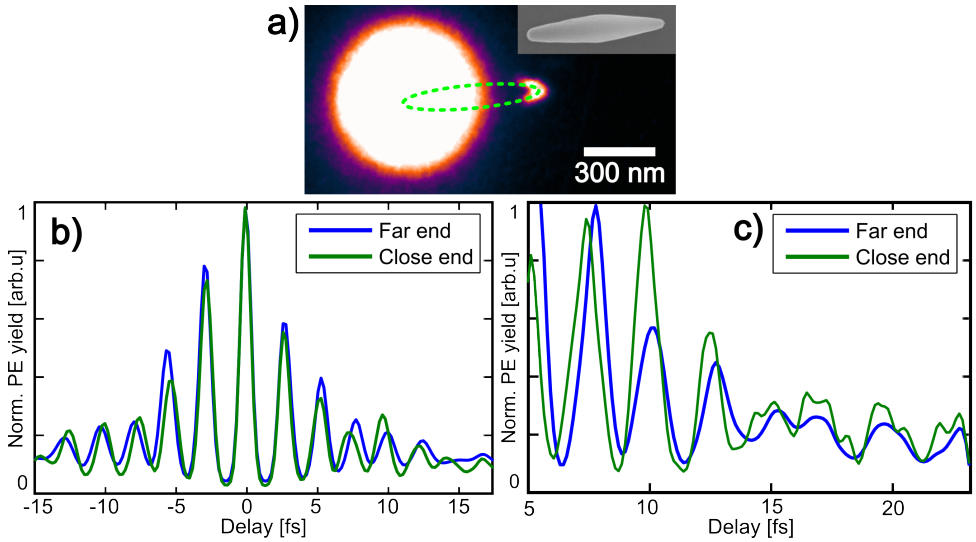

Figure 4.14: a) P–polarized IR image. Indent: SEM image of the same grain. b) Normalized near–field autocorrelation trace from the two ends. c) A second normalized near–field autocorrelation trace recorded using a smaller time–step centered around the de–phasing region. Already at a delay of 5 fs (2π), a shift between the two ends can be observed.

This type of measurement was repeated for different nanograins of varying length, and a consistent detectable shift could be distinguished in the delay range ($\pm$) 5–15 fs, with a magnitude of roughly ($\pm$) 200 as. The shift can always be seen on both sides of the central overlap of the autocorrelation trace and is sometimes constant until it either returns to oscillate in phase or is swallowed by noise. Since the two pulses of the interferometer are identical, the shift indicates that it is something inherent to the near–fields on the structure. However, worth noting is that they never go completely out of phase. These shifts imply that the near–field dynamics are being resolved on a sub–3 fs timescale.

4.3.2 FDTD simulations

Much like the procedure described in section 4.2.2, FDTD simulations modeled after the experimental setup were carried out in order to facilitate analysis of the measured data. Again, using the commercially available software FDTD Solutions by Lumerical, Inc., individual silver nanograins on a substrate were constructed. For consistency, the same excitation pulse settings, dielectric function fitting, as well as mesh grid size that were described in section 3.4 were also used for the nanoellipsoids. Fig. 4.15a–b) show a 500 nm long and 100 nm thick grain seen from two different angles. For simplicity, the long–axis of the nanoparticle was kept lying in the plane of incidence for all simulations.

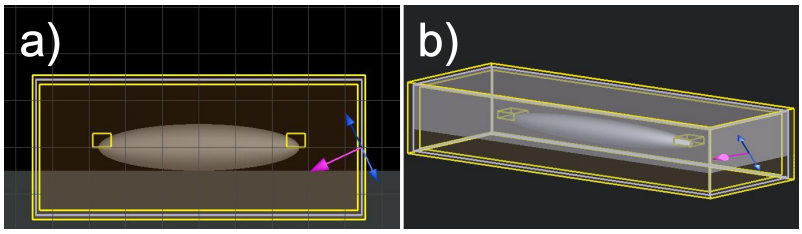

Figure 4.15: a–b) Ag nanograin, as seen from a few different angles. The arrows indicate incident angle and polarization of the excitation source.

Additionally, the dependence of resonance frequencies on nanograin length was investigated through a simulation parameter sweep. For nanograin lengths spanning 350 to 600 nm in steps of 50 nm at a constant thickness of 100 nm, FDTD simulations were carried out using otherwise the same settings as described earlier. Fig. 4.16a) shows the resulting absorption cross–sections for the nanograin length sweep. The dotted lines indicate how each mode red–shifts for increasing nanograin length. The DFT field distributions for the three modes present within the spectral range are shown in fig. 4.16b–d), evaluated at the frequencies indicated in fig. 4.16a). In order to highlight the in–phase oscillations of the longitudinal modes, only the z–component of the fields are shown in a plane normal to the plane of incidence. The numerical values indicated in the colorbars show the maximum E–field enhancement relative to the amplitude of the excitation pulse.

An estimate of what a PEEM image could look like was obtained by evaluating equation 2.7 for $n = 3$ in the plane of incidence for a 500 nm long grain, as shown in fig. 4.17a). Much like the grains imaged in the PEEM, the simulations predict a much greater photoemission response from the far end of the structure, even when only considering the z–component of the total electric field. Fig. 4.17b) shows the E_z–fields from each end of the grain as a function of time, while fig. 4.17c) shows the simulated autocorrelation trace from the response from evaluating equation 3.2. The electric field components for the two ends of the nanograins were recorded with volume sensors positioned on either end, as indicated by the yellow boxes in fig. 4.15a).

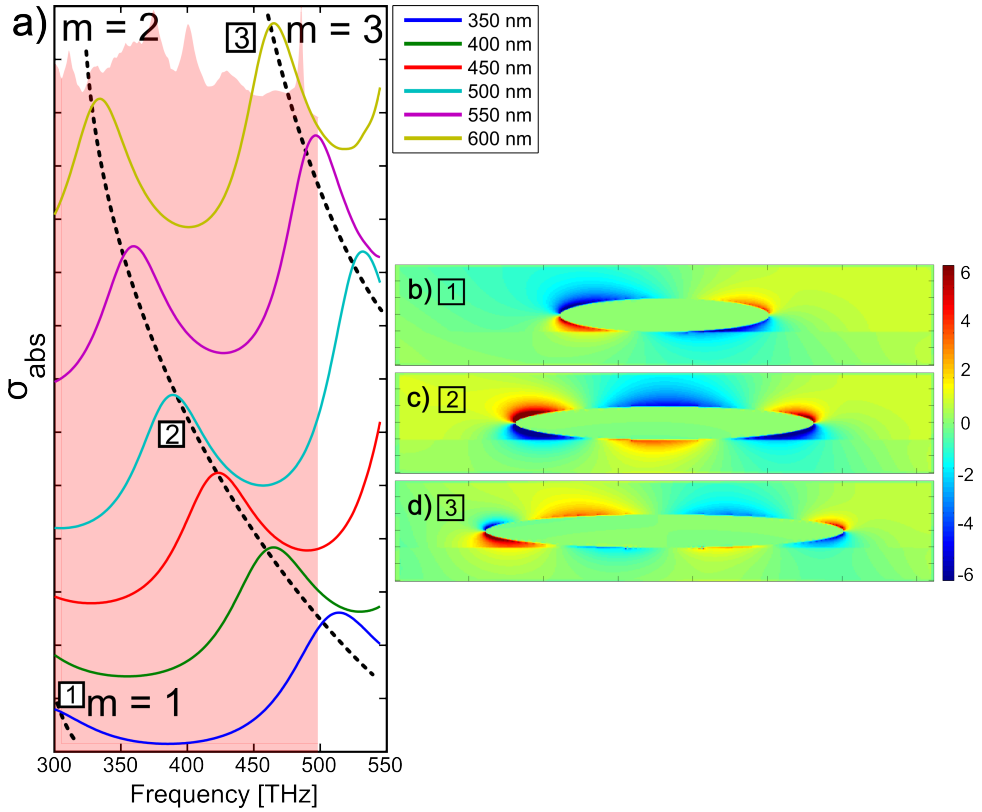

Figure 4.16: a) Absorption cross–sections for nanograins of different lengths. The dotted lines indicate how each mode red–shifts for increasing nanograin length and the red shaded area indicates the approximate spectral range of the laser pulses. E_z steady–state field distributions for the peaks marked 1 through 3, corresponding to the dipolar ($m = 1$), quadrupolar ($m = 2$) and octupolar ($m = 3$) mode, respectively, were evaluated at b) 300 THz for the 350 nm grain, c) 389 THz for the 500 nm grain and d) 465 THz for the 600 nm grain.

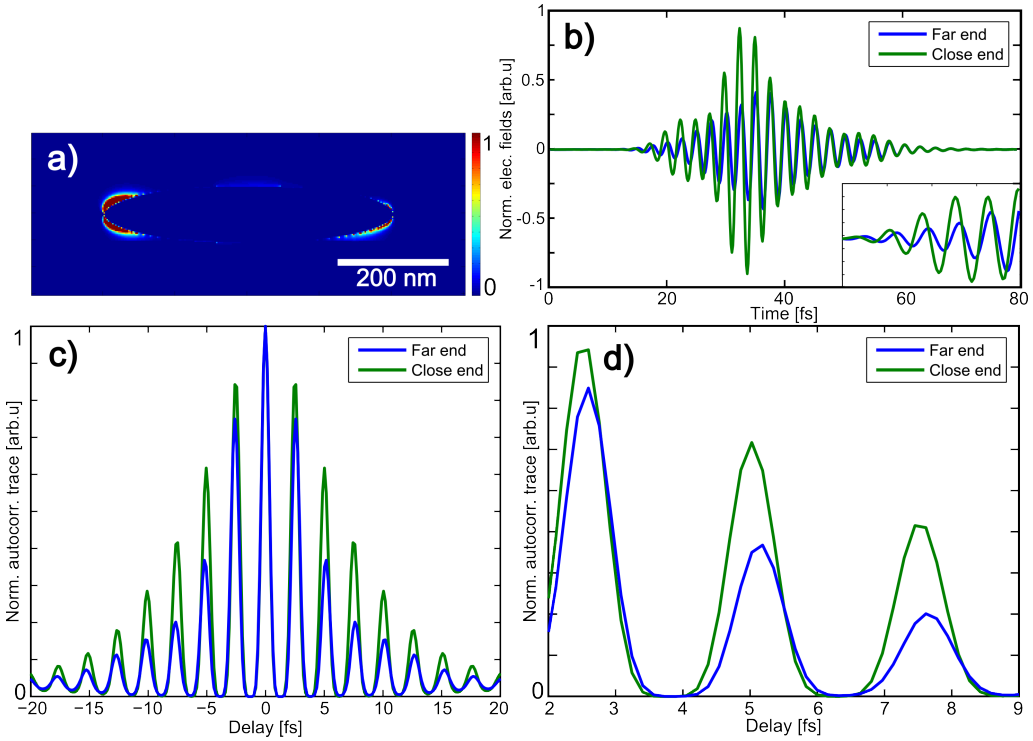

Figure 4.17: a) Simulated PEEM image of a 500 nm long nanograin for P–polarized excitation in the plane of incidence, normalized to 1. b) E_z response from each end. Inset: Zoom in on the first few cycles of the excitation build–up. c) Normalized simulated near–field autocorrelation trace. d) Zoom in on the de–phasing region of the simulated autocorrelation trace.

4.3.3 Looking into the autocorrelation dephasing

As have been shown in previous studies [25, 40], the grazing incidence of light pulses allows for the excitation of both even (dark) and odd (bright) longitudinal modes. This is supported through the simulated absorption spectra for grains of varying lengths shown in fig. 4.16, where multiple resonance peaks emerge within the spectral range of the laser pulses. Therefore, for certain geometries, one can expect a mixture of modes excited in the nanostructure at once.

Using the same argument as for the nanocubes, the amplitude of a peak in an absorption cross–section plot is directly related to how strongly a certain mode will be excited. Therefore, based on the absorption cross-sections shown in fig. 4.16a), arguably only the quadrupolar ($m = 2$) mode is excited for the 500 nm long grain. From the simulated near–field response from the two ends shown in fig. 4.17b), a de–phasing occurs during the build–up of the excitation. However, as soon as the excitation pulse has passed, the two ends can be seen to oscillate completely in phase. This can be explained through retardation effects, simply because the particle experiences a phase variation of the excitation light across its long axis. The phase variation is schematically illustrated in fig. 3.3b) by the laser pulse. This approach is further supported by the qualitative similarities in the de–phasing of the autocorrelation traces from the two ends for both PEEM measurements (fig. 4.14c)) and simulations (fig. 4.17d)).

However, the retardation approach is only valid for structures whose near–field enhancement is dominated by a single mode. It is worth noting here that the even quadrupolar mode ($m = 2$) is supported for all nanograin lengths that were considered, while the odd dipolar ($m = 1$) and octupolar ($m = 3$) modes are only supported for the shortest and longest nanograins, respectively. Thus, the total near–field for a given structure will be a coherent superposition of modes supported by that specific nanograin length. Because of this, as soon as two or more modes with different parity are excited at once, together with the retardation effects, a complicated beating pattern will emerge in the near–field response. However, the analysis of the what exactly is giving rise to the observed de–phasing phenomena for a mixture of even and off modes is currently a work in progress [41], and will not be discussed further.

Chapter 5

Summary and conclusion

During the course of this project, two separate types of silver nanostructures were studied. More specifically, nanocubes and ellipsoids resembling grains of rice. The method that was employed consisted of exciting plasmon resonances in the nanostructures using IR laser pulses as short as 5.5 fs and subsequently study the MPPE in a PEEM.

In contrast to earlier work, the current study allowed single particles to be measured, rather than an ensamble. This removed the shrouding effects often associated with averaged signals, enabling the observation of details such as orientation dependence and localized field enhancements. This is achieved by recording electrons, for the spatial resolution, emitted by interactions with photons, for the temporal resolution. Additionally, the high spatiotemporal resolution allowed the detection of the near–field distribution within a single particle.

For the nanocubes, the most striking result was the observation of near–field enhancements being confined to specific corners of the cube depending on the polarization of the grazing incident light. Earlier studies have shown similar results both experimentally for milled slits in a metallic substrate [42], circular Ag islands [24], the gaps between Au nanobars [43], and theoretically for the gaps between a trimer of Au nanospheres [44]. They all show that control of the far–field excitation allows direct manipulation of the plasmonic response in a manner that results in specific regions having enhanced localized fields. We experimentally demonstrate that this is also possible within the confines of an individual sub–wavelength structure. Depending on the polarization of the incident light, near–field enhancement can be induced in specific corners separated by ~ 250 nm. A qualitative model based on charge distribution interaction mechanisms, supported by

FDTD electrodynamics simulations, was employed to describe the observed phenomenon.

For the nanograins, MPPE could be observed from different ends of single particles. The MPPE was measured as a function of delay between two 5.5 fs laser pulses. It was experimentally demonstrated that a de–phasing occurs between the autocorrelation traces from the two ends of a particle. The observed shift in the autocorrelation traces implied that the near–field dynamics were being resolved in real–time on a sub–3 fs timescale, which was made possible due to the ultrashort laser pulses. For the case of a single mode, the shift was explained as an effect due to plasmon retardation across the particle caused by asymmetric excitation. This hypothesis was further supported by FDTD electrodynamics simulations of similar geometries.

For both the nanocubes and nanograins, even though different mechanics were observed, their behaviour could qualitatively be explained by models based on the excitation, or superposition, and modes supported within the spectral range of the laser pulses.

In conclusion, we show that a combination of photoemission electron microscopy and ultrashort laser pulses allows for the characterization of the spatial and temporal confinement of near–fields excited due to localized surface plasmon resonances. Additionally, we show that by merely controlling the far–field excitation, coherent control of the response can be established. This has implications for many plasmonic systems where control of the near-fields is desired. We further show that while many interactions at these time– and length–scales usually are very hard to interpret, different methods can be employed to partially understand them, such as the finite–difference time–domain method.

5.1 Outlook and further research

While interferometric pump–probe measurements can provide some insight into the dynamics of LSPs, true time–resolved measurements are not possible with the current setup. Since the temporal resolution of a pump–probe measurement is directly proportional to the pulse length of the probe pulse, an experimental setup using extreme ultraviolet (UV) attosecond pulses for probing is currently underway. Hopefully, such a setup will allow the mapping of real–time dynamics of the propagating SPPs, instead of the time–integrated response currently obtained by using IR probe pulses.

Bibliography

[1] R. H. Ritchie, "Plasma losses by fast electrons in thin films," *Physical Review*, vol. 106, no. 5, p. 874, 1957.

[2] A. Otto, "Excitation of nonradiative surface plasma waves in silver by the method of frustrated total reflection," *Zeitschrift für Physik*, vol. 216, no. 4, pp. 398–410, 1968.

[3] E. Kretschmann and H. Reather, "Radiative decay of nonradiative surface plasmon excited by light," *Z. Naturf.*, vol. 23A, pp. 2135–2136, 1968.

[4] R. P. Feynman, "There's Plenty of Room at the Bottom," *Engineering and Science*, vol. 23, no. 5, pp. 22–36, 1960.

[5] C. K. Chen, T. F. Heinz, D. Ricard, and Y. R. Shen, "Surface-enhanced second-harmonic generation and Raman scattering," *Physical Review B*, vol. 27, no. 4, p. 1965, 1983.

[6] E. Kirsten, G. Parschau, K. H. Rieder, W. H. Ehsasi, J. H. Block, and M. M. Löber, "Probing Single Molecules and Single Nanoparticles by Surface-Enhanced Raman Scattering," *Phys. Rev. B*, vol. 50, p. 2548, 1994.

[7] D. L. Jeanmaire and R. P. van Duyne, "Surface Raman Spectroelectrochemistry," *J. Electroanal. Chem.*, vol. 84, pp. 1–20, 1977.

[8] B. J. Wiley, S. H. Im, Z.-Y. Li, J. McLellan, A. Siekkinen, and Y. Xia, "Maneuvering the Surface Plasmon Resonance of Silver Nanostructures through Shape-Controlled Synthesis," *The Journal of Physical Chemistry B*, vol. 110, pp. 15666–15675, Aug. 2006.

[9] T. H. Maiman, "Stimulated Optical Radiation in Ruby," *Nature*, vol. 187, no. 5, pp. 493–494, 1960.

[10] A. Kubo, K. Onda, H. Petek, Z. Sun, Y. S. Jung, and H. K. Kim, "Femtosecond Imaging of Surface Plasmon Dynamics in a Nanostructured Silver Film," *Nano Lett.*, vol. 5, no. 6, pp. 1123–1127, 2005.

[11] H. Hertz, "Ueber einen Einfluss des ultravioletten Lichtes auf die electrische Entladung," *Annalen der Physik*, vol. 267, no. 8, pp. 983–1000, 1887.

[12] Accessed May 10, 2015. The Nobel Prize in Physics 1921, *http://www.nobelprize.org/nobel_prizes/physics/laureates/1921/*.

[13] M. G. Papadopoulos, A. J. Sadlej, and J. Leszczynski, *Non-Linear Optical Properties of Matter: From molecules to condensed phases*. Springer, 2007.

[14] U. Kreibig and M. J. Vollmer, *Optical Properties of Metal Clusters*. Springer, 1995.

[15] W. L. Barnes, A. Dereux, and T. W. Ebbesen, "Surface plasmon subwavelength optics," *Nature*, vol. 424, no. 6950, pp. 824–830, 2003.

[16] V. Giannini, A. I. Fernández-Domínguez, S. C. Heck, and S. A. Maier, "Plasmonic Nanoantennas: Fundamentals and Their Use in Controlling the Radiative Properties of Nanoemitters," *Chemical Reviews*, vol. 111, pp. 3888–3912, June 2011.

[17] C. L. Haynes and R. P. Van Duyne, "Nanosphere Lithography: A Versatile Nanofabrication Tool for Studies of Size-Dependent Nanoparticle Optics," *The Journal of Physical Chemistry B*, vol. 105, pp. 5599–5611, June 2001.

[18] H. Ditlbacher, A. Hohenau, D. Wagner, U. Kreibig, M. Rogers, F. Hofer, F. R. Aussenegg, and J. R. Krenn, "Silver Nanowires as Surface Plasmon Resonators," *Physical Review Letters*, vol. 95, Dec. 2005.

[19] G. Mie, "Beiträge zur Optik trüber Medien, speziell kolloidaler Metallösungen," *Annalen der Physik*, vol. 330, no. 3, pp. 377–445, 1908.

[20] K. S. Kunz and R. J. Luebbers, *The Finite Difference Time Domain Method for Electromagnetics*. CRC Press LLC, 1993.

[21] J. B. Schneider, "Understanding the finite-difference time-domain method," *School of electrical engineering and computer science Washington State University*, 2010.

[22] K. S. Yee, "Numerical solution of initial boundary value problems involving Maxwell's equations in isotropic media," *IEEE Trans. Antennas Propag*, vol. 14, no. 3, pp. 302–307, 1966.

[23] Accessed May 10, 2015, *http://fdtd.wikispaces.com/The+Yee+Cell*.

[24] M. Aeschlimann, M. Bauer, D. Bayer, T. Brixner, F. J. García de Abajo, W. Pfeiffer, M. Rohmer, C. Spindler, and F. Steeb, "Adaptive subwavelength control of nano-optical fields," *Nature*, vol. 446, pp. 301–304, Mar. 2007.

[25] H. Wei, A. Reyes-Coronado, P. Nordlander, J. Aizpurua, and H. Xu, "Multipolar Plasmon Resonances in Individual Ag Nanorice," *ACS Nano*, vol. 4, pp. 2649–2654, May 2010.

[26] Focus GmbH, Omicron NanoTechnology, *Instruction Manual Focus PEEM*, version 2.2 2007.

[27] Focus GmbH, Omicron NanoTechnology, *Instruction Manual Mercury Arc UV source*, 2005.

[28] M. Miranda, C. L. Arnold, T. Fordell, F. Silva, B. Alonso, A. L'Huillier, and H. Crespo, "Characterization of broadband few-cycle laser pulses with the d-scan technique," *Optics express*, vol. 20, no. 17, pp. 18732–18743, 2012.

[29] E. D. Palik, "Handbook of Optical Constants of Solids," *Academic*, 1985.

[30] H. Liang, H. Yang, W. Wang, J. Li, and H. Xu, "High-Yield Uniform Synthesis and Microstructure-Determination of Rice-Shaped Silver Nanocrystals," *Journal of the American Chemical Society*, vol. 131, pp. 6068–6069, May 2009.

[31] M. Chelvayohan and C. H. B. Mee, "Work function measurements on (110), (100) and (111) surfaces of silver," *J. Phys. C: Solid State Phys.*, vol. 15, pp. 2305–2312, Sept. 1982.

[32] J. P. Kottmann, O. J. F. Martin, D. R. Smith, and S. Schultz, "Plasmon resonances of silver nanowires with a nonregular cross section," *Physical Review B*, vol. 64, Nov. 2001.

[33] F. Zhou, Z.-Y. Li, Y. Liu, and Y. Xia, "Quantitative Analysis of Dipole and Quadrupole Excitation in the Surface Plasmon Resonance of Metal Nanoparticles," *The Journal of Physical Chemistry C*, vol. 112, pp. 20233–20240, Dec. 2008.

[34] E. Ringe, J. M. McMahon, K. Sohn, C. Cobley, Y. Xia, J. Huang, G. C. Schatz, L. D. Marks, and R. P. Van Duyne, "Unraveling the Effects of Size, Composition, and Substrate on the Localized Surface Plasmon Resonance Frequencies of Gold and Silver Nanocubes: A Systematic Single-Particle Approach," *The Journal of Physical Chemistry C*, vol. 114, pp. 12511–12516, July 2010.

[35] A. Grubisic, E. Ringe, C. M. Cobley, Y. Xia, L. D. Marks, R. P. Van Duyne, and D. J. Nesbitt, "Plasmonic Near-Electric Field Enhancement Effects in Ultrafast Photoelectron Emission: Correlated Spatial and Laser Polarization Microscopy Studies of Individual Ag Nanocubes," *Nano Letters*, vol. 12, pp. 4823–4829, Sept. 2012.

[36] Q. Sun, K. Ueno, H. Yu, A. Kubo, Y. Matsuo, and H. Misawa, "Direct imaging of the near field and dynamics of surface plasmon resonance on gold nanostructures using photoemission electron microscopy," *Light: Science & Applications*, vol. 2, p. e118, Dec. 2013.

[37] A.-I. Henry, J. M. Bingham, E. Ringe, L. D. Marks, G. C. Schatz, and R. P. Van Duyne, "Correlated Structure and Optical Property Studies of Plasmonic Nanoparticles," *The Journal of Physical Chemistry C*, vol. 115, pp. 9291–9305, May 2011.

[38] J. M. McLellan, Z.-Y. Li, A. R. Siekkinen, and Y. Xia, "The SERS Activity of a Supported Ag Nanocube Strongly Depends on Its Orientation Relative to Laser Polarization," *Nano Letters*, vol. 7, pp. 1013–1017, Apr. 2007.

[39] L. Douillard, F. Charra, Z. Korczak, R. Bachelot, S. Kostcheev, G. Lerondel, P.-M. Adam, and P. Royer, "Short Range Plasmon Resonators Probed by Photoemission Electron Microscopy," *Nano Letters*, vol. 8, pp. 935–940, Mar. 2008.

[40] H. Liang, H. Zhao, D. Rossouw, W. Wang, H. Xu, G. A. Botton, and D. Ma, "Silver Nanorice Structures: Oriented Attachment-Dominated Growth, High Environmental Sensitivity, and Real-Space Visualization of Multipolar Resonances," *Chemistry of Materials*, vol. 24, pp. 2339–2346, June 2012.

[41] E. Mårsell, A. Losquin, R. Svärd, M. Miranda, C. Guo, A. Harth, E. Lorek, J. Mauritsson, C. L. Arnold, H. Xu, A. L'Huillier, and A. Mikkelsen, "Nanoscale imaging of local few-fs near-field dynamics within a single plasmonic nanoantenna," *Manuscript*, 2015.

[42] J. Le Perchec, P. Quémerais, A. Barbara, and T. López-Ríos, "Controlling Strong Electromagnetic Fields at Subwavelength Scales," *Physical Review Letters*, vol. 97, July 2006.

[43] G. Volpe, S. Cherukulappurath, R. Juanola Parramon, G. Molina-Terriza, and R. Quidant, "Controlling the Optical Near Field of Nanoantennas with Spatial Phase-Shaped Beams," *Nano Letters*, vol. 9, pp. 3608–3611, Oct. 2009.

[44] A. Devilez, B. Stout, and N. Bonod, "Mode-balancing far-field control of light localization in nanoantennas," *Physical Review B*, vol. 81, June 2010.